Mon. Not. R. Astron. Soc. **000**, 1–21 (2010) Printed 23 July 2010 (MN LATEX style file v2.2)

Balancing Outflows and Gas Dilution: The Mass-Metallicity Relation at $z = 0$

Molly S. Peeples[1⋆] & Francesco Shankar[2]†
[1]*Department of Astronomy and Center for Cosmology and Astro-Particle Physics, Ohio State University, 140 W. 18th Ave., Columbus, OH 43210*
[2]*Max-Planck-Institüt für Astrophysik, Karl-Schwarzschild-Str. 1, D-85748, Garching, Germany*

23 July 2010

ABSTRACT

We present a new formalism with which to understand the relation between galaxy stellar mass and gas-phase oxygen abundance that explicitly considers the mass-dependence of galaxy gas fractions and outflows. By assuming that galaxies populate zero-scatter relations between their stellar masses, gas fractions, metallicities, outflow efficiencies, and halo properties, we show that if metal-accretion is negligible, then a galaxy's gas-phase metallicity $Z_{\rm g}$ can be simply expressed as $Z_{\rm g} = y[\zeta_{\rm w} + \alpha F_{\rm g} + 1]^{-1}$, where y is the nucleosynthetic yield, $\zeta_{\rm w}$ is a term describing the efficiency with which the galaxy expels its metals, $F_{\rm g}$ is the gas-to-stellar mass ratio, and α is a factor of order unity. We apply this formalism to $z \sim 0$ observations to show that reproducing observed oxygen abundances simultaneously with observed galaxy gas fractions requires efficient outflows. Without winds, models that match the mass-metallicity relation have $F_{\rm g} \gtrsim 0.3$ dex higher than observed. Moreover, gas fractions at $z = 0$ are small enough the mass-metallicity relation does not depend sensitively on the exact slope of the $F_{\rm g}$-$M_\star$ relation. Successful models require metal-expulsion efficiencies that are high and scale steeply with mass. Specifically, most reasonable models require $\zeta_{\rm w} > 1$ and $\zeta_{\rm w} \propto v_{\rm vir}^{-3}$ or steeper, where $\zeta_{\rm w} \equiv (Z_{\rm w}/Z_{\rm g})(\dot{M}_{\rm w}/\dot{M}_{\rm SFR})$ is the metallicity-weighted mass-loading parameter, $Z_{\rm w}$ is the metallicity of the outflowing material, $\dot{M}_{\rm w}$ is the mass outflow rate, and $\dot{M}_{\rm SFR}$ is the star formation rate. If the unweighted mass-loading factor $\eta_{\rm w} \equiv \dot{M}_{\rm w}/\dot{M}_{\rm SFR}$ scales as $v_{\rm vir}^{-1}$ or $v_{\rm vir}^{-2}$ as has been suggested from momentum- or energy-driven models, then a steep mass-dependence of $\zeta_{\rm w}$ implies that the $Z_{\rm w}$-$M_\star$ relation should be shallower than the $Z_{\rm g}$-$M_\star$ relation.

Key words: ISM: abundances — ISM: jets and outflows — galaxies: abundances — galaxies: evolution — galaxies: fundamental parameters — galaxies: ISM

1 INTRODUCTION

Star-forming galaxies follow a tight (~ 0.1 dex scatter) correlation between their gas phase oxygen abundance (hereafter referred to as "metallicity") and stellar mass (Tremonti et al. 2004). This mass-metallicity relation is primarily understood to be a sequence of oxygen *suppression*, rather than enrichment (Tremonti et al. 2004; Dalcanton 2007; Erb 2008; Finlator & Davé 2008). The production of oxygen traces the production of stars, implying that the observed trend in the oxygen-to-gas ratio reflects either a trend in the galaxy gas-to-stellar mass ratio or in processes that affect gas-phase metals but not stars. If the mass-metallicity relation is governed by an underlying trend in gas fractions, then the metals in low-mass galaxies are more diluted than in more massive galaxies because of the relatively larger gas fractions in the smaller galaxies (Garnett 2002; Leroy et al. 2008). Such preferential dilution can be attributed to variations in gas accretion and/or star formation efficiency with galaxy mass. On the other hand, large-scale galaxy winds affect galaxies' gas (and thus gas-phase metals) while not affecting the stars; if outflows are more efficient at removing metals from low-mass galaxies than more massive ones due to the less massive galaxies' relatively shallow potential wells, then the lower-mass galaxies will have lower metallicities (Wyse & Silk 1985; Heckman et al. 2000). In this paper, we present a comprehensive approach to modelling the mass-metallicity relation, incorporating both mass-dependent outflows and gas fractions.

Previous analytic studies have reached conflicting conclusions on the relative importance to the mass-metallicity relation of galaxy outflows and gas dilution. Focusing on the $z \sim 2.2$ mass-metallicity relation observed by Erb et al. (2006a), Erb (2008) used a simple analytic chemical evolution model to argue that the star formation rate, $\dot{M}_{\rm SFR}$, and the outflow rate, $\dot{M}_{\rm w}$, should be roughly equal. While $\dot{M}_{\rm w}$ and the gas accretion rate $\dot{M}_{\rm acc}$ vary with the star formation rate (and thus gas fraction), $\eta_{\rm w} \equiv \dot{M}_{\rm w}/\dot{M}_{\rm SFR}$ and

⋆ E-mail: molly@astronomy.ohio-state.edu
† E-mail: shankar@mpa-garching.mpg.de

$\eta_{\rm a} \equiv \dot{M}_{\rm acc}/\dot{M}_{\rm SFR}$ are constant universal parameters, a common practice in analytic models of galaxy chemical evolution (see also Samui et al. 2008, and references therein). Though models specifically aimed at duplicating observations of the mass-metallicity relation commonly assume $Z_{\rm w} = Z_{\rm g}$, Dalcanton (2007) argues that metal-enriched outflows (those comprised predominantly of Type II supernova ejecta, and thus with $Z_{\rm w} > Z_{\rm g}$) are required if the rate of gas accretion is to be reasonable. Several analytic models focus on the efficiency of star formation as a function of stellar mass. In the context of the mass-metallicity relation, variations in the star formation efficiency affect galaxy gas fractions (as well as the $M_\star$-$M_{\rm halo}$ relation). In such models, an increase in the star formation efficiency with galaxy mass—without the need for outflows—is sufficient to reproduce the observed mass-metallicity relation (Calura et al. 2009).

The mass-metallicity relation has also been studied in detail in several cosmological hydrodynamic simulations. Brooks et al. (2007) used a set of smoothed particle hydrodynamics (SPH) simulations evolved with Gasoline (Wadsley et al. 2004) to argue that preferentially expelling gas from the low-mass galaxies is insufficient for reproducing the observed mass-metallicity relation. These authors claim that it is instead the reduced star-formation efficiency (and thus differences in galaxy gas fractions) induced by such feedback that is primarily responsible for driving the relation's morphology. Conversely, Finlator & Davé (2008) used a suite of SPH simulations evolved with GADGET-2 (Springel 2005)—and therefore a different recipe for star-formation feedback[1] than Brooks et al. (2007)—in conjunction with detailed analytic models to show that, in general, $Z_{\rm g} \propto \eta_{\rm w}^{-1}$ for $\eta_{\rm w} \gg 1$. Their favored model that reproduces the Erb et al. $z \sim 2.2$ mass-metallicity relation is one in which $\eta_{\rm w} \propto \sigma^{-1}$, where σ is the galaxy velocity dispersion.[2] In this simulation, $\sigma^{-1} \propto M_{\rm halo}^{-1/3} \propto M_\star^{-1/3}$, which naturally explains why this $\eta_{\rm w}$ scaling is able to reproduce a mass-metallicity relation with $Z_{\rm g} \propto M_\star^{0.3}$. These simple scaling relations highlight a link between a galaxy's stellar mass, its halo mass, and its potential well: wind models aimed at successfully reproducing the mass-metallicity relation also need to correctly reproduce (or incorporate) the $M_\star$-$M_{\rm halo}$ relation.

A final class of models invokes a change in the galactic stellar initial mass function (GSIMF). The initial mass function (IMF) affects the mass-metallicity relation via the nucleosynthetic yield, i.e., the amount of oxygen (produced in Type II supernovae; Wallerstein 1962) made per mass of stars (see appendix A for a more thorough discussion). If, for example, the IMF is top-light in low-mass globular clusters, and massive clusters are not found in low mass galaxies, then low mass galaxies will simply produce less oxygen per unit stars than more massive galaxies, leading to a mass-metallicity relation like the observed one (Köppen et al. 2007). Similarly, while Calura & Menci (2009) use a hierarchical galaxy formation model to show that the mass-metallicity relation can be reproduced by assuming that a substantial fraction of the heavy elements is lost through metal-enhanced outflows in low mass galaxies, these authors also point out that a varying GSIMF helps in reproducing other observables, such as the $[\alpha/{\rm Fe}]$-σ relation in ellipticals (see also Recchi et al. 2009, and references therein).

These apparently conflicting results highlight several issues surrounding the origin of the mass-metallicity relation. First, a model that successfully reproduces the observed mass-metallicity relation does *not* uniquely constrain the relation's origin: gas dilution and galaxy outflows can be combined in a variety of ways—ranging from no preferential dilution to no preferential mass loss—to yield the same mass-metallicity relation. The question is what combinations of outflows and dilution can match the observed relation. Second, models must be constrained by observed gas fractions, not by the mass-metallicity relation alone. Finally, a fully consistent model of the mass-metallicity relation must allow for the fact that both galaxy gas fractions and galaxy outflow properties vary (as theory predicts and observations demonstrate) with galaxy mass. Furthermore, the way in which these properties depend on the galaxy mass may be more directly related to the galaxy's host halo's mass or velocity structure (such as the virial velocity or escape velocity). The origin of the mass-metallicity relation can then be constrained by appealing to external constraints set by observations of galaxy gas fractions and the empirically derived $M_\star$-$M_{\rm halo}$ relation. Here we present a new formalism for understanding the mass-metallicity relation that straightforwardly addresses these issues and apply it to the observed $z \sim 0$ mass-metallicity relation, where these external constraints are well measured.

Our approach is straightforward: we assume that galaxies populate a hypersurface describing their stellar and gas masses, halo properties, and metallicities. Observationally, Mannucci et al. (2010) and Lara-López et al. (2010) have recently shown that $Z_{\rm g}$ has less scatter at fixed $M_\star$ and $\dot{M}_{\rm SFR}$ than at just fixed $M_\star$ (i.e., the mass-metallicity relation); there is no evidence for evolution of this surface up to $z \sim 2.5$. This finding implies that the $M_\star$-$\dot{M}_{\rm SFR}$-$Z_{\rm g}$ hypersurface provides a more physical description of the underlying physics than just the $M_\star$-$Z_{\rm g}$ plane. In our formalism, the star formation rate is closely linked with outflow efficiencies, and observationally, gas fractions and star formation rates are tightly correlated. We calculate the relevant hypersurface by expressing the time evolution of a galaxy's stellar mass, gas mass, and gas-phase metallicity ($\dot{M}_\star$, $\dot{M}_{\rm g}$, and $\dot{Z}_{\rm g}$, respectively) in terms of each piece's possible sources and sinks (e.g., star formation, outflows, accretion). As detailed in § 3.1, the time dependence in these equations can be eliminated by dividing by the star formation rate to give the ${\rm d}Z_{\rm g}/{\rm d}M_\star$ differential, which, once integrated, is the mass-metallicity relation. By assuming that as galaxies grow in stellar mass they stay along mean relations, we require that the mass-metallicity relation depends only on instantaneous galaxy properties, such as gas masses and outflow efficiencies. In this paper, we apply this formalism to the observed $z \sim 0$ mass-metallicity relation, where these other externally constrained mean relations are best understood.

This paper is organized as follows. In §2, we discuss the relevant observations: those of the $z = 0$ mass-metallicity relation (§2.1), galaxy gas fractions (§2.2), and galaxy outflows (and theoretical models thereof, §2.3). We lay out our formalism in §3.1, along with how we connect galaxy stellar masses to host halo properties (§3.2). In §4, we show how gas dilution and outflows must combine in order to yield the observed mass-metallicity relation, and what this implies about galaxy outflows in order for predicted

[1] Because of the resolution of cosmological SPH simulations, star-formation feedback must be included using "recipes" instead of directly modelling the underlying physics. The winds in Finlator & Davé's simulations are implemented by physically moving gas particles away from star-forming regions. In Brooks et al.'s simulations, star formation thermally heats neighboring particles. In both prescriptions, the relevant particles are not allowed to interact hydrodynamically (Finlator & Davé) or radiatively cool (Brooks et al.) for some physically-motivated amount of time.

[2] This parameterization is motivated by the observations of Martin (2005) and the theory of momentum-driven winds (Murray et al. 2005); see §2.3 for more details.

ID	a	b	c	d
T04	$\mathbf{-0.759210}$	$\mathbf{1.30177}$	$\mathbf{0.003261}$	$\mathbf{-0.00364112}$
Z94	73.0539	-20.9053	2.23299	-0.0783089
KK04	28.1404	-7.02595	0.812620	-0.0301508
KD02	28.4613	-7.32158	0.855119	-0.0318315
M91	46.1480	-12.3801	1.33589	-0.0471074
D02	$\mathbf{-8.91951}$	$\mathbf{4.18231}$	$\mathbf{-0.323383}$	$\mathbf{0.00818179}$
PP04O3N2	32.5769	-8.61049	0.981780	-0.0359763
PP04N2	24.1879	-5.69253	0.648668	-0.0235065

Table 1. Kewley & Ellison (2008) fits to the mass-metallicity relation, where $\log Z_{\rm g} = a + b \log M_\star + c(\log M_\star)^2 + d(\log M_\star)^3$, sorted by decreasing $\max(Z_{\rm g})$. The two fits we consider in the main text (T04 and D02) are in bold. See text for abbreviations.

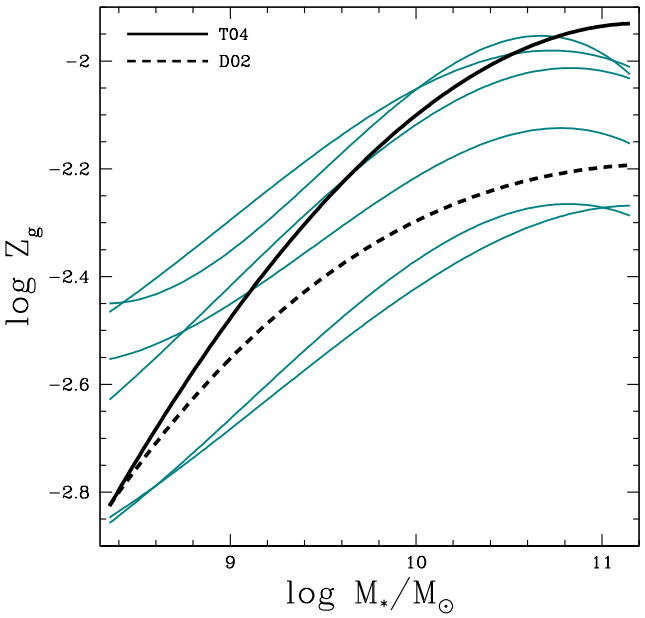

Figure 1. Mass-metallicity relations listed in Table 1 (Kewley & Ellison 2008, and equation 1). The scatter about any given one of these curves is 0.1–0.15 dex, which is much less than the differences in normalization; that is, the normalization differences are systematic. The mass-metallicity relations in black (T04, solid; D02, dashed) are modeled in detail §§ 4 and 5.

gas fractions to be consistent with the data. We then present in §5 what constraints wind metallicity and entrainment fraction considerations place on viable outflow models, with a summary and further discussion in §6 . Appendix A gives a detailed discussion of the definition of the nucleosynthetic yield, which sets the amplitude of the mass-metallicity relation. Appendix B describes the connection between gas masses, accretion, and star formation rates in our formalism, with implications for star formation efficiency.

Throughout we adopt a cosmology of $(\Omega_m, \Omega_b, \sigma_8, h) = (0.26, 0.047, 0.77, 0.72)$ and a Chabrier (2003a) initial mass function (IMF), unless otherwise noted. We note here that varying the cosmological parameters, within the ranges allowed from observations (e.g., Hinshaw et al. 2009), does not alter our conclusions. The impact of varying Ω_m or Ω_b, has, for example, little effect on the shape of the $M_\star$-$M_{\rm halo}$ relation or on the determination of the stellar masses in SDSS. Though varying σ_8 does change the number density of massive halos, it has little impact on the range of halo masses of interest here. Finally, we note that the virial relations only have a mild change in normalization when varying cosmological parameters, without having much impact on our overall results.

2 RELEVANT OBSERVATIONS

2.1 The observed $z \sim 0$ mass-metallicity relation

It is difficult—if not impossible—to measure the gas phase abundances of all of the elements not made in the Big Bang, i.e., true gas phase metallicities. Oxygen-to-hydrogen abundance ratios in H II regions, however, are relatively straightforward to estimate. Since oxygen is effectively produced only in Type II SNe—the deaths of massive, short-lived stars—and H II regions are associated with ongoing star formation, the gas-phase "mass-metallicity relation" typically refers to only the galaxy's oxygen abundance in gas that is currently forming stars; we therefore will use "metals" and "oxygen" interchangeably unless otherwise noted. However, though $12 + \log({\rm O/H})$ is measured at the sites of star formation, the measured abundances are the *birth* abundances of the H II regions; supernovae (the sites of oxygen production) destroy their nascent clouds, rendering so-called "self enrichment" of H II regions extremely rare. We therefore also assume that the galaxy gas is well-mixed, i.e., that the mixing time is short relative to the timescale for star formation.

Observationally, oxygen abundance increases with galaxy stellar mass. This relation has very little scatter ($\sim$ 0.1 dex in $12 + \log[{\rm O/H}]$ at fixed stellar mass), though severe outliers do exist (Peeples et al. 2008, 2009). The amplitude and slope of the mass-metallicity relation, however, are not well constrained, despite exquisite and extensive data (e.g., from the Sloan Digital Sky Survey [SDSS]; Adelman-McCarthy et al. 2006). This ambiguity is due to the theoretical uncertanties in how to convert emission-line fluxes to $12 + \log({\rm O/H})$, as one must make assumptions about both the gas temperature and ionization structure in order to derive $\log({\rm O/H})$. While the electron temperature can be estimated directly using the [O III] $\lambda 4363$ auroral line, this line is extremely weak and usually only detectable in very metal-poor environments. Thus, it is common to calibrate measurement methods using much stronger forbidden emission lines such as [O II] $\lambda\lambda 3726, 3729$, H$\beta$, [O III] $\lambda\lambda 4959, 5007$, H$\alpha$, and [N II] $\lambda 6584$ based on the so-called direct [O III] $\lambda 4363$ T_e method. However, since [O III] $\lambda 4363$ preferentially emits in high-temperature regions, this calibration can lead to an over-estimate of the electron temperature based on this line and thus an under-estimate of the oxygen abundance (Kewley & Ellison 2008). It is therefore common to instead calibrate strong-line measurement methods based on theoretical photoionization models. On the other hand, there are arguments that such strong-line methods *over*-estimate the true abundance (Kennicutt et al. 2003). In addition to these problems, most indicators are either double-valued at low metallicities (such as the popular R_{23} indicator) or saturate at high metallicites as emission-line cooling shifts to the near-infrared (e.g., Bresolin 2006).

Kewley & Ellison (2008) highlight many of these issues, and derive $12 + \log({\rm O/H})$ for a large set of galaxies from SDSS using ten indicators (eight of which we consider here: T04, Tremonti et al. 2004; D02, Denicoló et al. 2002; KK04, Kobulnicky & Kewley 2004; Z94, Zaritsky et al. 1994; KD02, Kewley & Dopita 2002; M91, McGaugh 1991; PP04O3N2 and PP04N2, using the Pettini & Pagel 2004 ([O III]/Hβ)/([N II]/Hα) and [N II]/Hα flux ratios, respectively). The Kewley & Ellison fits

to the mass-metallicity relation are given in Table 1, where we have converted from a Kroupa (2001) to a Chabrier (2003a) IMF and from $12 + \log(\mathrm{O/H})$ to $\log Z_\mathrm{g}$, where

$$\begin{aligned} \log Z_\mathrm{g} &= [12 + \log(\mathrm{O/H})] - 12 - \log\left[\frac{M_\mathrm{O}/M_\mathrm{H}}{XM_\mathrm{H} + YM_\mathrm{He}}\right] \quad (1) \\ &= \log(\mathrm{O/H}) - \log\left[\frac{15.999/1.0079}{0.75 \times 1.0079 + 0.25 \times 4.0026}\right]. \end{aligned}$$

These mass-metallicity relations are plotted in Figure 1; the scatter in Z_g at fixed $M_\star$ for each mass-metallicity relation is smaller by a factor of 2–3 than the spread in normalizations, implying that the differences are caused by the systematics discussed above.

The two relations in black in Figure 1 and in bold in Table 1 (T04, Tremonti et al. 2004 and D02, Denicoló et al. 2002) are the two mass-metallicity relations we focus on in § 4. While we do not favor any one $12 + \log(\mathrm{O/H})$ indicator, we take these two mass-metallicity relations as representative of the normalizations and slopes observations as a whole. The D02 indicator is a linear relation between the [N II] λ6584/Hα ratio and $12 + \log(\mathrm{O/H})$calibrated against T_e metallicities. The relatively low normalization of this method is common for T_e-calibrated indicators. The T04 method is based on theoretical stellar population synthesis and photoionization models combined with a Bayesian analysis of many more strong emission lines than used in most methods.

2.2 Observed gas fractions of $z \sim 0$ galaxies

Figure 2 shows how the gas-to-stellar mass ratio F_g (left panel) and gas mass M_g (right panel) vary with galaxy stellar mass. The open diamonds are total H I gas masses measured from 21 cm line fluxes (McGaugh 2005). The crosses are also H I gas masses, with stellar masses measured from SDSS (Garcia-Appadoo et al. 2009; West et al. 2009, 2010). The filled circles represent the total H I + H_2 gas masses (including a correction for helium) from The H I Nearby Galaxy Survey (THINGS), with the H_2 masses derived from HERA CO-Line Extragalactic Survey (HERACLES) and the Berkeley-Illinois-Maryland Association Survey of Nearby Galaxies (BIMA SONG) CO measurements (Leroy et al. 2008). Though there is large scatter in the gas fraction at a fixed stellar mass, gas fractions clearly decrease as $M_\star$ increases; this behavior is also found in cosomological hydrodynamic simulations (e.g., Hopkins et al. 2008). The mean $\log F_\mathrm{g}$ in bins of $\Delta \log M_\star = 0.4$ dex for $8.1 \leqslant \log M_\star \leqslant 11.3$ is overplotted with the large solid orange squares; we list these means and uncertainties in Table 2. We note that each of these data sets focus on star-forming galaxies similar to those in which $12 + \log(\mathrm{O/H})$ is measurable; surveys not restricted to actively star-forming galaxies (e.g., Catinella et al. 2010) lead to much lower average gas fractions.

We parameterize F_g as power-law of the form

$$F_\mathrm{g} \equiv \frac{M_\mathrm{g}}{M_\star} = \left(\frac{M_\star}{M_{\star,0}}\right)^{-\gamma} = K_f M_\star^{-\gamma}, \quad (2)$$

with $\gamma > 0$. Table 3 lists $\log M_{\star,0}$, K_f and γ for our adopted gas relations. As we show in §3.1, F_g is a more convenient parameterization than the commonly used and more arguably intuitive μ_g, the gas mass as a fraction of the total baryonic galaxy mass $M_\star + M_\mathrm{g}$,

$$\mu_\mathrm{g} \equiv \frac{M_\mathrm{g}}{M_\mathrm{g} + M_\star} = \frac{F_\mathrm{g}}{1 + F_\mathrm{g}}. \quad (3)$$

The "total" gas fraction relation is a power-law fit to the combined

$\langle \log M_\star \rangle$	$\langle \log F_\mathrm{g} \rangle$	$\sigma_{\log F_\mathrm{g}}$
8.3298	0.5153	0.07867
8.7265	0.3084	0.06500
9.0892	0.2062	0.06359
9.5141	−0.07142	0.06220
9.8941	−0.3230	0.04817
10.298	−0.5548	0.06666
10.664	−0.8389	0.06212
11.053	−0.8303	0.06566

Table 2. Cold gas fractions $\log F_\mathrm{g} = \log(M_\mathrm{g}/M_\star)$ in bins of $\Delta \log M_\star = 0.4$ dex and the uncertainty in the mean $\sigma_{\log F_\mathrm{g}}$ for the McGaugh (2005), Leroy et al. (2008), and Garcia-Appadoo et al. (2009) data sets.

Name	$\log M_{\star,0}$	K_f	γ
Total	9.6	316228	0.57
SDSS	6.0	15.85	0.20
Fiber	2.7	2.24	0.13
Flat	—	0.50	0.00

Table 3. Gas fraction relation parameters, $F_\mathrm{g} = M_\mathrm{g}/M_\star = K_f M_\star^{-\gamma}$.

McGaugh, Leroy et al., and Garcia-Appadoo et al. data sets, offset by $+0.2$ dex so that the total gas fractions are greater than those implied by the K-S law (see below). In order to understand the contribution of a sloped gas fraction relation to the mass-metallicity relation, we also consider a flat gas relation of $M_\mathrm{g} = 0.5 M_\star$, shown in green in Figure 2.

For reference, Figure 2 shows how the total baryonic halo mass, $(\Omega_b/\Omega_m)M_\mathrm{h}$, varies with stellar mass (halo mass as a function of $M_\star$ is calculated as discussed in §3.2). The offset between the baryonic halo mass and $M_\star + M_\mathrm{g}$ is evidence of the so-called missing baryon problem; the missing baryons are either hot or have been expelled from the halos by $z = 0$ (e.g., Crain et al. 2007). Figure 2 further highlights the fact that for $M_\star \lesssim 10^{10}\,\mathrm{M}_\odot$, the fraction of baryons in the form of cold gas is roughly constant (i.e., the blue and red lines are roughly parallel). Moreover, while massive galaxies are gas poor, galaxies with stellar masses below $\sim 10^{9.5}\,\mathrm{M}_\odot$ have most of their mass in the form of gas: the processes responsible for the "missing baryons" in $z = 0$ halos must also account for this inefficiency of star formation in low mass halos. We discuss this issue further in Appendix B.

The Kennicutt-Schmidt (K-S, Kennicutt 1998; Schmidt 1959) law is commonly used to indirectly estimate gas masses in star-forming galaxies when direct gas masses are expensive (or currently impossible) to achieve, such as at high redshifts (e.g., Erb et al. 2006b) or for large samples of galaxies (e.g., Tremonti et al. 2004). Furthermore, since $12 + \log(\mathrm{O/H})$ is measured only in star-forming gas, it is reasonable to consider gas fractions that trace this same gas. The purple lines in Figure 2 are the gas masses we derive from applying the K-S law to star-forming Data Release 4 SDSS galaxies with z-band magnitude errors of < 0.01 mag (Brinchmann et al. 2004; Adelman-McCarthy et al. 2006). Specifically, we relate the star formation rate surface density Σ_SFR to the gas surface density Σ_g by

$$\Sigma_\mathrm{SFR} \equiv \frac{\dot{M}_\mathrm{SFR}}{A_g} = K_g \Sigma_g^\alpha \quad (4)$$

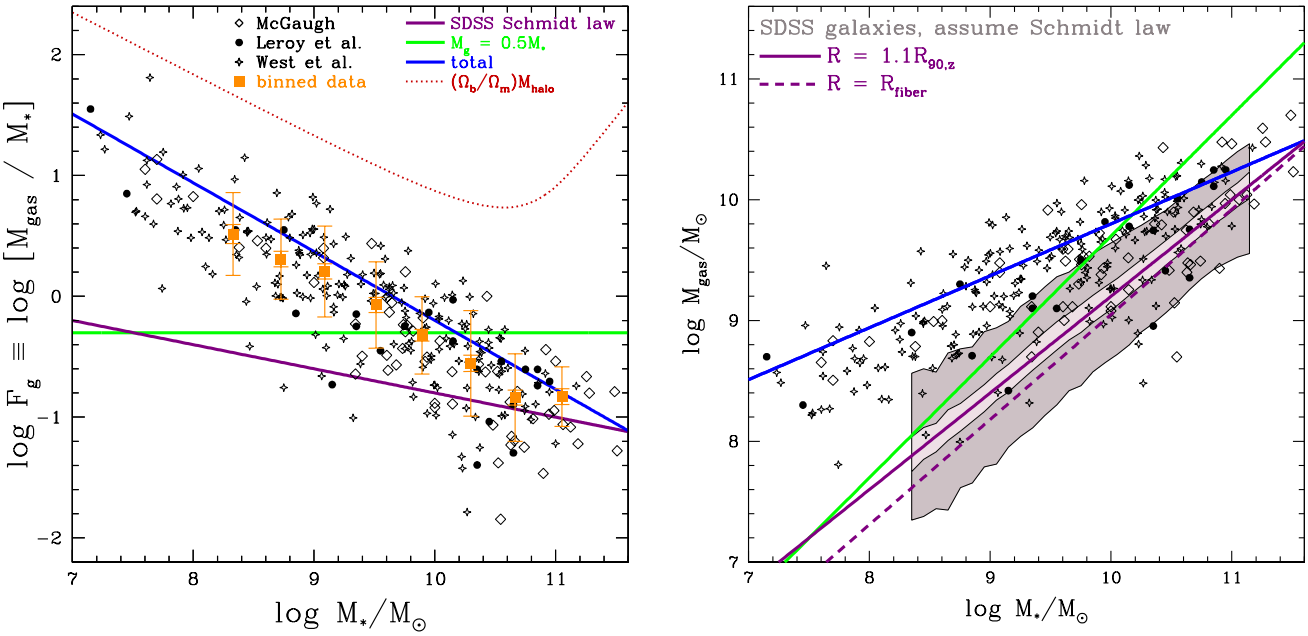

Figure 2. Left: Gas fractions $F_{\rm g}$ as a function of $M_\star$. Right: Gas masses $M_{\rm g}$ as a function of $M_\star$. The open black diamonds are H I gas fractions and masses from McGaugh (2005); the crosses are the same from West et al. (2009, 2010). The filled circles are H I + H_2 gas fractions and masses (Leroy et al. 2008), who find that there is very little H_2 below $\log M_\star \sim 9.5$, which is consistent with the comparison to the H I samples. The red dotted line shows the maximum baryonic mass $(\Omega_b/\Omega_m)M_{\rm halo}$, while the green "flat" line shows $M_{\rm g} = 0.5M_\star$. The blue "total" line is a fit to these data with the normalization increased by 0.2 dex; the orange squares are the mean $\log F_{\rm g}$ of these same data in bins of $\Delta \log M_\star = 0.4$ dex with the inner and outer errorbars denoting the uncertainty in and dispersion about the mean, respectively. Gas fractions and masses derived from SDSS data and inverting the K-S law, assuming a radius of $1.1R_{90,z}$ (solid line) and the fiber radius (dashed line); in the right panel, the shaded region corresponds to the 1- and 2-σ dispersions in moving bins of $\log M_\star$.

$$= \quad 1.67 \times 10^{-4} \left(\frac{\Sigma_g}{1 {\rm M}_\odot \ {\rm pc}^{-2}} \right)^{1.4} {\rm M}_\odot \ {\rm yr}^{-1} \ {\rm kpc}^{-2}$$

from Kennicutt (1998), where we have corrected for the fact that the Brinchmann et al. (2004) star formation rates are based on a Kroupa (2001) IMF while the Kennicutt relation is based on a Salpeter (1955) IMF. SDSS spectra are taken within a 3″ aperture; therefore, to measure *total* galaxy properties (e.g., star formation rates and stellar masses), the fact that the aperture does not subtend the entire galaxy must be corrected for. We therefore consider $\Sigma_{\rm SFR}$ and $M_\star$ both for the full galaxy-light radius (which we take to be 1.1 times the 90th percentile z-band isophotal radius $R_{90,z}$) and only within the fiber, i.e., we take

$$A_g = \pi R_g^2 = \pi R_{\rm light}^2 = \pi \times \left\{ \begin{array}{ll} 1.1^2 \times R_{90,z}^2; & \text{solid lines.} \\ R_{\rm fiber}^2; & \text{dashed line.} \end{array} \right. \quad (5)$$

The galaxy gas mass is then simply

$$M_{\rm g} = \left(\dot{M}_{\rm SFR} \times \frac{A_g^{\alpha-1}}{K_g} \right)^{1/\alpha} . \quad (6)$$

The shaded contours in the right panel of Figure 2 denote the 1-σ and 2-σ gas masses derived for the entire galaxy ($R_g = 1.1R_{90,z}$) in running bins of $\log M_\star$ from $\log M_\star = 8.3$ to 11.1; for clarity, galaxies falling outside this region are not shown. The solid line is an eyeball power-law fit to the median $R_g = 1.1R_{90,z}$ gas masses while the dashed line is the same for the gas (and stellar) masses within the SDSS fiber. The fact that these relations are quite similar to one another indicates that aperture corrections are relatively small and/or that gas fractions are relatively scale-invariant within $1.1R_{90,z}$.

The gas masses estimated from the K-S law and the measurements of total cold gas masses roughly agree with one another on the low gas fraction of $F_{\rm g} \sim 0.1$ at $\log M_\star \sim 11$, and that $F_{\rm g}$ increases with decreasing stellar mass. The amount of this increase in gas fraction, however, is in stark disagreement, with a range of over an order of magnitude in $F_{\rm g}$. The K-S law only traces star-forming gas and therefore traces molecular gas more closely than atomic, and dwarf galaxies are deficient in molecular gas (Leroy et al. 2008). At large radii in more massive galaxies, the gas is predominately atomic, i.e., the H I radii of galaxies is often much larger than the optical (star-forming) radii (Boomsma et al. 2008; Walter et al. 2008). For the purposes of the mass-metallicity relation, what matters is the total amount of gas that is able to effectively mix and dilute metals. A lower limit to this gas mass is the gas that is able to collapse and form stars—the gas traced by the K-S law. If on the other hand the atomic and molecular gas are well mixed (as opposed to, e.g., molecular gas only populating the galaxy center and atomic gas being at large radii), then the total gas fractions are more applicable. Finally, neither of these gas fraction estimates include ionized gas; if such gas is not only prevalent in typical galaxies but also has efficient mass transfer with both supernova ejecta and gas that will cool to form molecular clouds (and subsequently H II regions), then even the "total" gas fraction relation will be an underestimate of the gas diluting the galaxies' metals.

2.3 Galaxy outflows

Though observations of galaxy-scale outflows are notoriously difficult, galaxy winds observed in a range of star-forming galaxies display a complex, multiphase structure. Since detectability increases with the star formation rate density (Veilleux et al. 2005), however, the most detailed studies of galaxy winds have been of the outflows associated with extreme starbursts, namely, (ultra)luminous infrared galaxies ([U]LIRGs). Studies of blue-shifted absorption-lines reveal both neutral (Heckman et al. 2000; Rupke et al. 2002; Martin 2005) and photoionized gas (Grimes et al. 2009), often with several kinematically distinct components. In contrast, X-ray emission around local starbursts such as M82 indicates a hot ($T \sim 10^{6.5}$–10^{8} K), tenuous ($n \sim 10^{-4}$–$10^{-3}\,\mathrm{cm}^{-3}$) wind fluid (Strickland & Stevens 2000; Strickland & Heckman 2007, 2009). Wind velocities derived from both emission and absorption line studies are typically hundreds of $\mathrm{km\,s}^{-1}$ (Martin 2005; Grimes et al. 2009). The systemic outflow velocity of emitting regions in this coronal gas phase is found to be positively correlated with the ionization energy of the absorbing ion (Grimes et al. 2006), indicating the presence of a shock, though in some cases this has been interpreted as a possible AGN contribution to the outflow (Spoon & Holt 2009). The outflow velocity $v_{\rm w}$ of the colder neutral gas is typically comparable to one to a few times the galaxy's circular velocity $v_{\rm circ}$ (Martin 2005), which is comparable to the galaxy's virial velocity $v_{\rm vir}$ (e.g., Diemand et al. 2007).

The scaling $v_{\rm w} \sim v_{\rm vir}$ follows naturally if momentum transfer from radiation pressure is driving the wind (Murray et al. 2005). For radiation pressure to be effective, the starburst must be Eddington limited and the outflowing gas has an asymptotic velocity of

$$v_{\rm w}(\infty) = 2v_{\rm esc}\left(\frac{L}{L_{\rm edd}} - 1\right)^{1/2}, \tag{7}$$

where the escape velocity $v_{\rm esc}$ is comparable to the virial velocity. The wind velocity is therefore typically taken to be $v_{\rm w} = 3v_{\rm vir}$. In the single-scattering limit (Murray et al. 2005),

$$\dot{M}_{\rm w} v_{\rm w} = \frac{L_{\rm starburst}}{c} = \frac{\epsilon_{\rm nuc}\dot{M}_{\rm SFR}c^2}{c}, \tag{8}$$

where $L_{\rm starburst}$ is the starburst luminosity and $\epsilon_{\rm nuc} = 8 \times 10^{-4}$ is the nuclear burning efficiency. Thus the mass-loading factor[3] $\eta_{\rm w}$ is proportional to the inverse of the virial velocity such that

$$\eta_{\rm w}\Big|_{\rm momentum} \equiv \frac{\dot{M}_{\rm w}}{\dot{M}_{\rm SFR}} = \frac{\epsilon_{\rm nuc}c}{v_{\rm w}} \sim \frac{80\,\mathrm{km\,s}^{-1}}{v_{\rm vir}}. \tag{9}$$

This same scaling is achieved if the wind is driven by cosmic rays (Socrates et al. 2008).

On the other hand, the outflow may be driven by energy transfer, perhaps from supernovae thermally heating the ISM (Chevalier & Clegg 1985; Dekel & Silk 1986; Silk & Rees 1998; Murray et al. 2005). In this popular scenario,

$$\frac{1}{2}\dot{M}_{\rm w}v_{\rm w}^2 \approx \xi E_{\rm SN} \times [\#\text{ of SNe per solar mass of stars formed}]\dot{M}_{\rm SFR}, \tag{10}$$

where $E_{\rm SN} \sim 10^{51}$ erg is the typical energy per supernova and ξ is the efficiency with which supernovae transfer energy to the ISM. Letting $\xi = 0.1$, i.e., a 10% efficiency, and taking the number of supernovae per unit mass to be 10^{-2}, this yields a mass-loading factor of

$$\eta_{\rm w}\Big|_{\rm energy} \equiv \frac{\dot{M}_{\rm w}}{\dot{M}_{\rm SFR}} \sim \left(\frac{73\,\mathrm{km\,s}^{-1}}{v_{\rm vir}}\right)^2, \tag{11}$$

where we have implicity assumed $v_{\rm w} \approx 3v_{\rm vir}$. While we in general consider models in which $\eta_{\rm w} \propto v_{\rm vir}^{-\beta}$ for $\beta > 0$ (or, equivalently, $\eta_{\rm w} \propto M_{\rm halo}^{-\beta/3}$, see §3.2); it is helpful to keep the normalizations suggested by equations (9) and (11) in mind.

Except via the impact of outflows on galaxy gas fractions, the mass-metallicity relation is insensitive to the *total* mass outflow rate $\dot{M}_{\rm w}$. Instead, as we show in §3.1, oxygen depletion due to winds is governed by the rate of metal loss, $Z_{\rm w}\dot{M}_{\rm w}$, where $Z_{\rm w}$ is the metallicity of the outflow; in our case (see §2.1), the mass ratio of oxygen in the outflowing material. While many metals (oxygen, as well as, e.g., iron, sodium, carbon, magnesium, and neon; Heckman et al. 2000; Martin 2005; Strickland & Heckman 2007; Martin & Bouché 2009; Grimes et al. 2009; Spoon & Holt 2009) are observed in galaxy outflows, there are relatively few observations of outflowing oxygen, and elemental abundances in the wind fluid are rarely reported. Strickland & Heckman (2009), however, find that the X-ray emitting outflow from M82 has a high enough metal content that it is consistent with containing nearly all of the freshly produced metals in the starburst with an inferred velocity of $\sim$ 1000–2000 $\mathrm{km\,s}^{-1}$. Combined with their interpretation that the outflow has very little entrained gas (i.e., that it is essentially comprised solely of supernova ejecta), this implies that the metallicity of the outflow is quite high. (We note that in this interpretation of the data, supernova explosions surprisingly have no radiative energy losses when interacting with the ambient ISM [$\xi = 1$ in equation 10]; see also Heckman 2003.) This picture is further complicated by the fact that outflows are likely multi-phase, and the metallicities and escape fractions in, e.g., the cold and ionized phases may be different. From the perspective of the mass-metallicity relation, however, what matters is the total amount of expelled oxygen relative to the total amount of expelled gas, where "expelled" oxygen or gas is just the oxygen or gas that has either been physically ejected from the galaxy or simply heated up such that it cannot efficiently transfer mass to the gas that is able to cool and form stars and thus be observed contributing to the mass-metallicity relation.

[3] Definitions in the literature of the "mass-loading factor" vary; we take it to mean the *total* outflow mass rate divided by the *total* star formation rate (including short-lived stars).

3 THE FORMALISM

3.1 The mass-metallicity relation

The three galaxy masses relevant to the mass-metallicity relation are the total galaxy mass in stars, $M_\star$, the galaxy gas mass, $M_{\rm g}$, and the mass of gas-phase metals, M_Z. We base our model on relating the instantaneous change in these masses via their sources and sinks to the instantaneous galaxy star formation rate, $\dot{M}_{\rm SFR}$, ignoring environmental effects such as mergers and tidal stripping. The instantaneous change in the stellar mass,

$$\dot{M}_\star = \dot{M}_{\rm SFR} - \dot{M}_{\rm recy} \tag{12}$$

$$= \dot{M}_{\rm SFR}(1 - f_{\rm recy}), \tag{13}$$

is given by the creation of stars ($\dot{M}_{\rm SFR}$) and the rate at which stars return mass to the ISM when they die, $\dot{M}_{\rm recy}$. (We include the mass of stellar remnants in $M_\star$.) The relative rate of these two effects, $f_{\rm recy} \equiv \dot{M}_{\rm recy}/\dot{M}_{\rm SFR}$, depends on the star formation history and therefore varies somewhat with time; its effect on our results, how-

ever, is small, and we are safe to adopt $f_{\rm recy} = 0.2$. (See Appendix A for a more thorough discussion of $f_{\rm recy}$.)

The gas mass is also regulated by the star formation rate and $f_{\rm recy}$, with gas accretion adding gas and outflows removing gas from the system. The instantaneous change in $M_{\rm g}$ is therefore

$$\dot{M}_{\rm g} = \dot{M}_{\rm acc} - \dot{M}_{\rm SFR} + \dot{M}_{\rm recy} - \dot{M}_{\rm w} \quad (14)$$

$$= \dot{M}_{\rm SFR}(\eta_{\rm a} - 1 + f_{\rm recy} - \eta_{\rm w}), \quad (15)$$

where $\dot{M}_{\rm acc}$ is the gas accretion rate and $\dot{M}_{\rm w}$ is the mass rate of outflowing gas. As introduced in §2.3, we define the mass-loading factor $\eta_{\rm w}$ as $\dot{M}_{\rm w}/\dot{M}_{\rm SFR}$; analogously, $\eta_{\rm a} \equiv \dot{M}_{\rm acc}/\dot{M}_{\rm SFR}$. The sources and sinks of metals are essentially the same as for gas, except that each component can have a different metallicity. Hence,

$$\dot{M}_Z = Z_{\rm IGM}\dot{M}_{\rm acc} - Z_{\rm g}\dot{M}_{\rm SFR} + Z_{\rm ej}\dot{M}_{\rm recy} - Z_{\rm w}\dot{M}_{\rm w} \quad (16)$$

$$= \dot{M}_{\rm SFR}(y + Z_{\rm g}(\zeta_{\rm a} - \zeta_{\rm w} - 1)), \quad (17)$$

where $Z_{\rm IGM}$ is the metallicity of accreting gas, $Z_{\rm g}$ is the ISM metallicity, $Z_{\rm ej}$ is the metallicity of gas being returned to the ISM by dying stars, and $Z_{\rm w}$ is the metallicity of outflowing gas. The yield y is the nucleosynthetic yield, which is defined as the rate at which metals are being returned to the ISM relative to the current star formation rate, i.e.,

$$y = \frac{\dot{M}_{\rm new\ metals}}{\dot{M}_{\rm recy}} \times \frac{\dot{M}_{\rm recy}}{\dot{M}_{\rm SFR}} = Z_{\rm ej} f_{\rm recy}. \quad (18)$$

After the first generation of Type II supernovae explode ($\sim 10^7$ yr), y is constant for continuous star formation. The IMF and Type II supernova yields, however, are highly uncertain, so the true value of y is only constrained to be $0.08 \lesssim y \lesssim 0.023$ (e.g., Finlator & Davé 2008); we adopt a mid-range value of $y = 0.015$. (See Appendix A for more details.)

The metallicity-weighted mass-loading factors $\zeta_{\rm a}$ and $\zeta_{\rm w}$ in equation (17) describe the relative rates at which metals are being accreted and expelled from the system, and are defined as

$$\zeta_{\rm a} \equiv \frac{Z_{\rm IGM}}{Z_{\rm g}} \times \frac{\dot{M}_{\rm acc}}{\dot{M}_{\rm SFR}} = \left(\frac{Z_{\rm IGM}}{Z_{\rm g}}\right)\eta_{\rm a}, \text{ and} \quad (19)$$

$$\zeta_{\rm w} \equiv \frac{Z_{\rm w}}{Z_{\rm g}} \times \frac{\dot{M}_{\rm w}}{\dot{M}_{\rm SFR}} = \left(\frac{Z_{\rm w}}{Z_{\rm g}}\right)\eta_{\rm w}. \quad (20)$$

The metallicity of accreting gas, $Z_{\rm IGM}$, is typically taken to be zero, though SPH simulations indicate that due to previous episodes of enrichment of the intergalactic medium (IGM) from metal-containing galaxy outflows, the effective $Z_{\rm IGM}$ may be non-negligible (Finlator & Davé 2008; Oppenheimer et al. 2009). Because a self-consistent model of an enriched IGM will be based on the evolution of the mass-metallicity relation, we will for now take $Z_{\rm IGM}$ and thus $\zeta_{\rm a} = 0$, though we will return to the ramifications of this assumption in § 6.3. The wind metallicity, $Z_{\rm w}$, is often assumed to be the ISM metallicity (Finlator & Davé 2008; Erb 2008), giving $\zeta_{\rm w} = \eta_{\rm w}$. However, $Z_{\rm g}$ is simply a lower-limit to the possible outflow metallicity (if the wind is driven by supernovae, then it can be metal-enriched relative to the ambient ISM, but not metal-depleted). The actual wind metallicity will depend on the fraction $f_{\rm e}$ of the outflow that is entrained interstellar gas, which has a generic metallicity $Z_{\rm g}$, and the fraction $1 - f_{\rm e}$ that is from newly exploded supernovae and therefore has a metallicity $Z_{\rm ej,max} \sim 0.1$ (see Appendix A). The wind metallicity is thus

$$Z_{\rm w} = (1 - f_{\rm e})Z_{\rm ej,max} + f_{\rm e}Z_{\rm g}, \quad (21)$$

where we note that $f_{\rm e}$ may vary with galaxy mass and must satisfy $0 \leqslant f_{\rm e} < 1$.

Since we are interested in the mass-metallicity relation at $z = 0$, and not its rate of change, it is useful to eliminate the time-dependence in equations (12–17). We assume galaxies live on a hypersurface of $M_{\rm g}$, $M_\star$, $Z_{\rm g}$, halo, accretion and wind properties. Dividing out the time-dependence in these equations allows us to solve for the shape of this surface, with observations setting the amplitude. Combining equations (13) and (15),

$$\frac{{\rm d}M_{\rm g}}{{\rm d}M_\star} = \frac{\eta_{\rm a} - \eta_{\rm w} - 1 + f_{\rm recy}}{1 - f_{\rm recy}} = F_{\rm g}(1 - \gamma), \quad (22)$$

where we include ${\rm d}M_{\rm g}/{\rm d}M_\star = F_{\rm g}(1 - \gamma)$ based on our parameterization of $F_{\rm g} = M_{\rm g}/M_\star$ (equation 2) introduced in §2.2. Note that if we assume we know how gas fractions vary with stellar mass (§2.2), then for any given wind model $\eta_{\rm w}$, the accretion rate as a function of the star formation rate $\eta_{\rm a}$ is uniquely determined. We explore this point and its implications in Appendix B.

The rate of change of the gas phase metallicity $Z_{\rm g}$ is

$$\dot{Z}_g = \frac{\rm d}{{\rm d}t}\frac{M_Z}{M_{\rm g}} = \frac{\dot{M}_Z}{M_{\rm g}} - \frac{Z_{\rm g}}{M_{\rm g}}\dot{M}_{\rm g} = \frac{1}{M_{\rm g}}\left[\dot{M}_Z - Z_{\rm g}\dot{M}_{\rm g}\right]. \quad (23)$$

We can now combine equations (13), (15), (17), and (23) to find

$$\frac{{\rm d}Z_{\rm g}}{{\rm d}M_\star} = \frac{y + Z_{\rm g}\left(\zeta_{\rm a} - \zeta_{\rm w} - 1 - \dfrac{\dot{M}_{\rm g}}{\dot{M}_{\rm SFR}}\right)}{M_{\rm g}(1 - f_{\rm recy})} \quad (24)$$

$$= \frac{y + Z_{\rm g}[\zeta_{\rm a} - \zeta_{\rm w} - 1 - F_{\rm g}(1 - \gamma)]}{M_{\rm g}(1 - f_{\rm recy})}. \quad (25)$$

Equation (24) can be integrated with respect to $M_\star$ to find $Z_{\rm g}(M_\star)$. Furthermore, using the Kewley & Ellison (2008) fits (§ 2.1, Table 1), we can turn the problem around: by assuming we know the mass-metallicity relation (and ${\rm d}Z_{\rm g}/{\rm d}M_\star$), we can infer the required relation between, e.g., $F_{\rm g}$ and $\zeta_{\rm w}$. Specifically, by rearranging equation (24), we find

$$Z_{\rm g} = y\Bigg[\zeta_{\rm w} - \zeta_{\rm a} + F_{\rm g}(1 - f_{\rm recy})\left(\frac{{\rm d}\log M_{\rm g}}{{\rm d}\log M_\star} + \frac{{\rm d}\log Z_{\rm g}}{{\rm d}\log M_\star}\right) + 1\Bigg]^{-1} \quad (26)$$

$$= y\left[\zeta_{\rm w} - \zeta_{\rm a} + \alpha F_{\rm g} + 1\right]^{-1}, \quad (27)$$

where

$$\alpha \equiv (1 - f_{\rm recy})\left(\frac{{\rm d}\log M_{\rm g}}{{\rm d}\log M_\star} + \frac{{\rm d}\log Z_{\rm g}}{{\rm d}\log M_\star}\right) \quad (28)$$

is a factor of order unity. Equation (27) is the mass-metallicity relation; by finding combinations of the yield, outflow strength, and gas fractions that combine as stated on the right-hand side to give $Z_{\rm g}(M_\star)$ on the left-hand side, we can explicitly reproduce the observed mass-metallicity relation. This is the tack we take in § 4.

3.2 Connecting galaxies and halos

A number of methods have been developed to empirically connect galaxies to halos. One straightforward approach is the cumulative matching of galaxy ($n_{\rm gal}$) and halo ($n_{\rm halo}$) number counts (e.g., Vale & Ostriker 2004; Shankar et al. 2006; Conroy & Wechsler 2009), i.e.,

$$n_{\rm gal}(> M_\star) = n_{\rm halo}(> M_{\rm halo})\,. \quad (29)$$

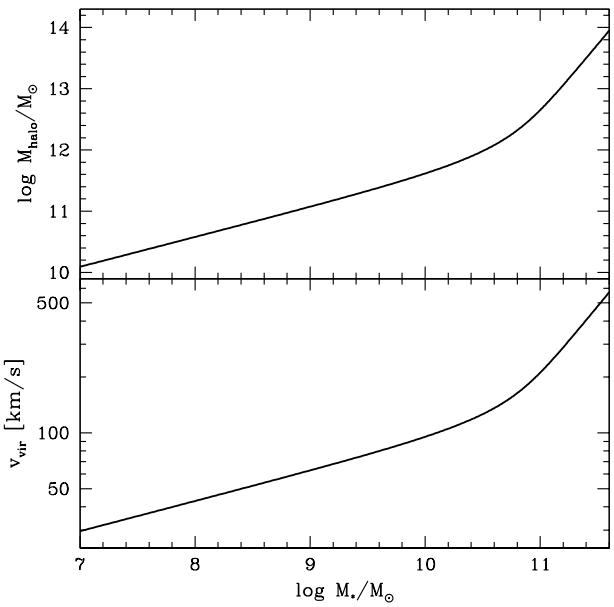

Figure 3. Halo mass, $M_{\rm halo}$, and virial velocity, $v_{\rm vir}$, as a function of stellar mass, $M_\star$, at $z = 0$ (Moster et al. 2009). See § 3.2 for more details.

Assuming that each halo (and subhalo) contains a galaxy, equation (29) determines the average mapping between halo mass and galaxy mass.

We adopt one of the latest determinations of the $M_\star$-$M_{\rm halo}$ relation by Moster et al. (2009, top panel of Figure 3),

$$\frac{M_\star}{M_{\rm halo}} = 0.0633(1+z)^{-0.72} \times \left[\left(\frac{M_{\rm halo}}{M_{\rm h,0}}\right)^{-1.06-0.17z} + \left(\frac{M_{\rm halo}}{M_{\rm h,0}}\right)^{0.556(1+z)^{-0.26}}\right]^{-1}, \quad (30)$$

with the zero point increased by 0.05 dex to correct from a Kroupa (2001) to a Chabrier (2003b) IMF (Bernardi et al. 2010), and where

$$\log M_{\rm h,0}/{\rm M}_\odot = [\log 11.88]\,(1+z)^{0.019}\,. \quad (31)$$

The Moster et al. (2009) $M_\star$-$M_{\rm halo}$ mapping is in good agreement with constraints from galaxy-galaxy lensing, galaxy clustering, and predictions of semi-analytic models. Following the scaling relations in Tonini et al. (2006, and references therein), we have verified that equation (31) yields a Tully-Fisher relation (Tully & Fisher 1977) consistent with the more recent calibrations by Pizagno et al. (2007), as long as the dynamical contribution of the dark matter within a few optical radii is less than the one predicted by a pure Navarro, Frenk, & White (1996) mass profile, in line with many other studies (e.g., Salucci et al. 2007). Also note that the subhalo masses quoted by Moster et al. refer to *unstripped* quantities, which represent more reliable indicators of the intrinsic potential well in which satellites formed.

The Moster et al. relation is in broad agreement with previous studies, such as the ones by Shankar et al. (2006), although the latter relied on a stellar mass function based on dynamical mass-to-light ratios that cannot be directly used in the present study based on SDSS stellar masses. Despite the different techniques adopted, most of the studies find consistent results on the $M_\star$-$M_{\rm halo}$ relation, especially in the mass range of interest here, i.e., star-forming galaxies with stellar mass $\lesssim 2\times10^{11}{\rm M}_\odot$ and hence halos with mass $\lesssim 5\times10^{12}\,h^{-1}{\rm M}_\odot$ (Firmani et al. 2009; More et al. 2010).

If winds depend on the potential well depth of the halo rather than the mass itself, then the halo virial velocity $v_{\rm vir}$ is more relevant than $M_{\rm halo}$. Roughly speaking,

$$v_{\rm vir}^2 \sim \Phi \sim \frac{GM_{\rm halo}}{R_{\rm halo}}, \quad (32)$$

where the dependence of the halo radius $R_{\rm halo}$ on the halo mass is a function of both cosmology and the structure of the halo (Łokas & Mamon 2001; Ferrarese 2002; Loeb & Peebles 2003; Baes et al. 2003). We connect $v_{\rm vir}$ to $M_{\rm halo}$ via

$$\begin{aligned} v_{\rm vir} &= \left(\frac{GM_{\rm halo}}{R_{\rm vir}}\right)^{1/2} \\ &= 112.6\left(\frac{M_{\rm halo}}{10^{12}\,{\rm M}_\odot}\right)^{1/3} \\ &\times \left[\frac{\Omega_m}{0.25}\frac{1}{\Omega_m^z}\frac{\Delta}{18\pi^2}\right]^{1/6}(1+z)^{1/2}\ {\rm km\,s^{-1}}, \end{aligned} \quad (33)$$

where the mean density contrast (relative to the critical density) within the virial radius $R_{\rm vir}$ is $\Delta = 18\pi^2 + 82d - 39d^2$, with $d \equiv \Omega_m^z - 1$, and $\Omega_m^z = \Omega_m(1+z)^3/\left[\Omega_m(1+z)^3+\Omega_\Lambda\right]$ (Bryan & Norman 1998; Barkana & Loeb 2001). The bottom panel of Figure 3 shows how $v_{\rm vir}$ varies with stellar mass in this model. We have verified that our $M_\star$-$v_{\rm vir}$ relation is in good agreement with the $M_\star$-v_{200} relation recently derived by Dutton et al. (2010a).

4 MODELS OF THE MASS-METALLICITY RELATION

We now turn to what is required to reproduce the observed mass-metallicity relation. Rearranging equation (27), we find

$$\frac{y}{Z_{\rm g}} - 1 = \zeta_{\rm w} - \zeta_{\rm a} + \alpha F_{\rm g}, \quad (34)$$

where we hereafter take $\zeta_{\rm a} = 0$ (see § 6.3 for a discussion of this choice). Expressed this way, the metallicity $Z_{\rm g}$ is related explicitly to a sum of $\zeta_{\rm w}$ (a term describing outflows) and $F_{\rm g} = M_{\rm g}/M_\star$ (a term describing the galaxy gas content). Equation (34), or equivalently equation (27), is the principal theoretical result of this paper, connecting gas-phase metallicities to gas fractions, outflows, and accretion. Functionally, one can use equation (34) to find working models for a given $Z_{\rm g}(M_\star)$ in several ways:

(i) Assume y and $Z_{\rm g}(M_\star)$ are known; use trial and error to find combinations of $\zeta_{\rm w}(v_{\rm vir})$ and $[\alpha F_{\rm g}](M_\star)$ that satisfy equation (34).

(ii) Assume y, $Z_{\rm g}(M_\star)$, and $\zeta_{\rm w}(v_{\rm vir})$ are known; solve for ${\rm d}\log M_{\rm g}/{\rm d}\log M_\star$ in equation (24) and integrate to find $M_{\rm g}(M_\star)$.

(iii) Assume y, $Z_{\rm g}(M_\star)$, and $M_{\rm g}(M_\star)$ are known; equation (34) then says $\zeta_{\rm w} = y/Z_{\rm g} - 1 - \alpha F_{\rm g}$.

Method (i) works well for developing intuition regarding tensions in the data and theoretical wind models, while methods (ii) and (iii) yield models that exactly produce the observed mass-metallicity relation, as demonstrated for the Tremonti et al. mass-metallicity relation in Figures 4 and 6. Best-fitting models of $\zeta_{\rm w}$ for the T04 mass-metallicity relation and relations based on other indicators (§ 2.1) are plotted in Figure 5–7 and tabulated in Table 4. In the top two panels of Figure 4, the observations are shown as the solid black curves; the colored lines denote models with different scalings of $\zeta_{\rm w}$ with $v_{\rm vir}$. Panel (a) shows the mass-metallicity relation

($\log Z_{\rm g}$ as a function of $\log M_\star$). The models are chosen so that they give $\zeta_{\rm w} + \alpha F_{\rm g}$ to equal the observed $y/Z_{\rm g} - 1$ (panel b). Gas fractions and $\zeta_{\rm w}(v_{\rm vir})$ are plotted in panels (c) and (d), respectively. Because of uncertainties in the nucleosynthetic yield, the normalization of the mass-metallicity relation, and possible saturation of metallicity indicators at high $12 + \log({\rm O/H})$ (see Appendix A and § 2.1), we will consider both the mass-metallicity relation across the mass range $8.1 \leqslant \log M_\star \leqslant 11.3$ and restricted to below $M_\star \sim 10.5\,{\rm M}_\odot$.

The gas fractions needed to dilute the metals in the absence of winds ($\zeta_{\rm w} = 0$) are shown as the solid orange line in Figure 4; these gas fractions are higher by a factor of $\gtrsim 3$ than observed cold gas fractions in typical $z \sim 0$ galaxies. For a non-varying yield, outflows are therefore required in order to keep the observed mass-metallicity relation consistent with galaxy gas fraction observations. This conclusion holds even more strongly for the other mass-metallicity relations plotted in Figure 1: in the absence of winds, lower metallicities imply higher gas fractions.

The other colored lines in Figure 4 show the required gas fractions if we assume $\zeta_{\rm w} = [50\,{\rm km\,s^{-1}}]/v_{\rm vir}$ (pink, long-dashed), $([85\,{\rm km\,s^{-1}}]/v_{\rm vir})^2$ (blue, short-dashed), or $([85\,{\rm km\,s^{-1}}]/v_{\rm vir})^3$ (green, dotted). Both the momentum-driven and energy-driven $\zeta_{\rm w}$ scalings require $F_{\rm g}$ to scale more steeply with mass than is observed; lower normalizations of $\zeta_{\rm w}$ force $F_{\rm g}$ to asymptote to the no winds case. A steeper scaling of $\zeta_{\rm w}$ with $v_{\rm vir}$, however, leads to more reasonable gas fractions.

We quantify what $\zeta_{\rm w}(v_{\rm vir})$ scalings are required in order to reproduce the mass-metallicity relation while remaining consistent with the observed gas fractions by using method (ii): by taking a given $\zeta_{\rm w}$ we can compare the corresponding $F_{\rm g}$ to binned gas fractions (§ 2.2, Table 2) to calculate a χ^2. Parameterizing $\zeta_{\rm w}$ as $(v_0/v_{\rm vir})^{-b} + \zeta_{\rm w,0}$, the best-fit model for the T04 mass-metallicity relation is $\zeta_{\rm w} = (78\,{\rm km\,s^{-1}}/v_{\rm vir})^{-3.81} + 0.19$, as shown in Figure 5. We show the $\Delta\chi^2$ contours for 1-, 2-, and 3-σ using the $\Delta\chi^2$-to-σ conversion from Press et al. (1992) for 5 degrees-of-freedom (8 data points and 3 parameters). The best-fit values do not change significantly if the dispersion about the mean is used instead of the uncertainties when calculating χ^2, and we safely consider the points and errors for the binned data to be uncorrelated because the measurements for individual galaxies do not depend on one another. Also, we choose to bin $F_{\rm g}$ instead of $Z_{\rm g}$ because the mass-metallicity relation has been more rigorously measured than the $F_{\rm g}$-$M_\star$ relation. The white regions in Figure 5 correspond to models that are unphysical because they require negative gas fractions. The best-fit models are always close to the border between physical and unphysical regions in parameter space, reflecting the fact that gas fractions at $z = 0$ are relatively small; it takes only a small change in $\zeta_{\rm w}$ to go from a small $F_{\rm g}$ to a negative one.

The best-fit $\zeta_{\rm w}$ can be strongly driven by the turnover of the mass-metallicity relation and change in slope of the $M_\star$-$v_{\rm vir}$ relation above $\log M_\star = 10.5$. For example, for the T04 mass-metallicity relation, if we instead only consider the data at $\log M_\star < 10.5$, the best-fit $\zeta_{\rm w}$ is instead $(72\,{\rm km\,s^{-1}}/v_{\rm vir})^{-4.69} + 0.41$; that is, the velocity normalization v_0 does not change much, but the slope steepens and the constant offset $\zeta_{\rm w,0}$ increases. Whether the best-fit $\zeta_{\rm w}$ shifts to higher b and $\zeta_{\rm w,0}$ (T04 and D02), lower b and $\zeta_{\rm w,0}$ (M91, Z94, PP04O3N2, and PP04N2), or doesn't change (KD02 and KK04) when only modeling $\log M_\star < 10.5$ depends on the subtle details of the particular fit to the mass-metallicity relation under consideration. In all cases, however, $\Delta\chi^2$ for the parameters for the best fitting $\zeta_{\rm w}$ for a given mass-metallicity relation when the entire mass range is modeled fall within 1-σ of the $\log M_\star < 10.5$ best fitting model for that indicator (but not necessarily vice-versa, since the best fitting low-mass model often requires negative gas fractions if extrapolated above $10^{10.5}{\rm M}_\odot$). The 1-σ range of $\zeta_{\rm w}$ for the T04 mass-metallicity relation is shown by the shaded yellow and beige regions in the right-hand panel of Figure 6 for the $\log M_\star < 10.5$ and entire mass range, respectively.

ID	v_0	b	$\zeta_{\rm w,0}$
T04	78.0	3.81	0.19
Z94	63.5	3.20	0.23
KK04	55.5	3.04	0.32
KD02	71.0	3.18	0.39
M91	73.0	2.47	0.77
D02	79.0	3.42	1.25
PP04O3N2	90.0	3.15	1.50
PP04N2	111.8	2.31	1.35

Table 4. Best-fit parameters for $\zeta_{\rm w} = (v_0/v_{\rm vir})^b + \zeta_{\rm w,0}$ the fits to the mass-metallicity relation calculated by Kewley & Ellison (2008) and listed in Table 1 and the binned gas fractions plotted in Figure 2. These $\zeta_{\rm w}$ are plotted next to the corresponding $Z_{\rm g}(M_\star)$ in Figure 7.

We turn this problem around in Figure 6 by considering $\zeta_{\rm w}(v_{\rm vir})$ while assuming $F_{\rm g}(M_\star)$ is known [method (iii)]. As discussed in § 2.2, we consider the total gas fractions (blue, solid lines), $M_{\rm g} = 0.05(\Omega_b/\Omega_m)M_{\rm halo}$ (red, dotted), gas fractions as inferred by inverting the Schmidt law for SDSS galaxies (purple), and $M_{\rm g} = 0.5M_\star$ (green). The $M_{\rm g} \propto M_{\rm halo}$ model is included because it might provide a natural explanation for the observed turnover in the mass-metallicity relation near M^*. We find that for the observed normalization of $F_{\rm g}(M_\star)$, the *slope* of the gas fraction relation is largely irrelevant in setting the mass-metallicity relation morphology. That is, $z = 0$ galaxies have little enough gas that the mass-metallicity relation is shaped by how $\zeta_{\rm w}$ rather than $F_{\rm g}$ scales with galaxy mass. This can be seen visually in the right-hand panel of Figure 6: at low masses, even the flat gas fraction relation has approximately the same $\zeta_{\rm w}$ slope as those models with steep $F_{\rm g}$-$M_\star$ relations.

Other metallicity indicators lead to mass-metallicity relations that are generally shallower and have a lower normalization than the Tremonti et al. mass-metallicity relation. This translates into $\zeta_{\rm w} + \alpha F_{\rm g}$ needing to be larger and to scale slightly less steeply with mass than seen in Figure 6; the best-fit $\zeta_{\rm w}$ for all of the mass-metallicity relations shown in Figure 1 are plotted in Figure 7. Detailed example models for the shallow, low-normalization Denicoló et al. (2002) mass-metallicity relation are shown in Figure 8. Numerically, observed gas fractions require $2.3 \lesssim b \lesssim 4$; this scaling with $v_{\rm vir}$ is much steeper than the canonical models for the unweighted mass-loading parameter discussed in § 2.3. Furthermore, $\zeta_{\rm w}$ must be large ($\gtrsim 1$) at all relevant masses. The only way around a large $\zeta_{\rm w}$ is if a significant fraction of the gas that is diluting the metals is ionized.

In the limit of small $F_{\rm g}$ and large $\zeta_{\rm w}$, one can see from equation (27) that $Z_{\rm g} \propto \zeta_{\rm w}^{-1}$ (Finlator & Davé 2008). We are using cubic fits to the mass-metallicity relation (Table 1, Kewley & Ellison 2008), but for the relevant mass range, the mass-metallicity relation has $0.2 \lesssim$ slope $\lesssim 0.45$ for most of the relations plotted in Figure 7. Our $M_\star$-$M_{\rm halo}$-$v_{\rm vir}$ relation (Figure 3) has $M_\star \propto v_{\rm vir}^6$ for $\log M_\star \lesssim 10$ (and $M_\star \propto v_{\rm vir}^{1.5}$ for $\log M_\star \gtrsim 10.6$). Thus, the metallicity $Z_{\rm g}$ is roughly proportional to $v_{\rm vir}^{1.2}$ to $v_{\rm vir}^{2.7}$, implying that for $\zeta_{\rm w} \propto v_{\rm vir}^{-b}$, b should be in the range 1.2 to 2.7. The

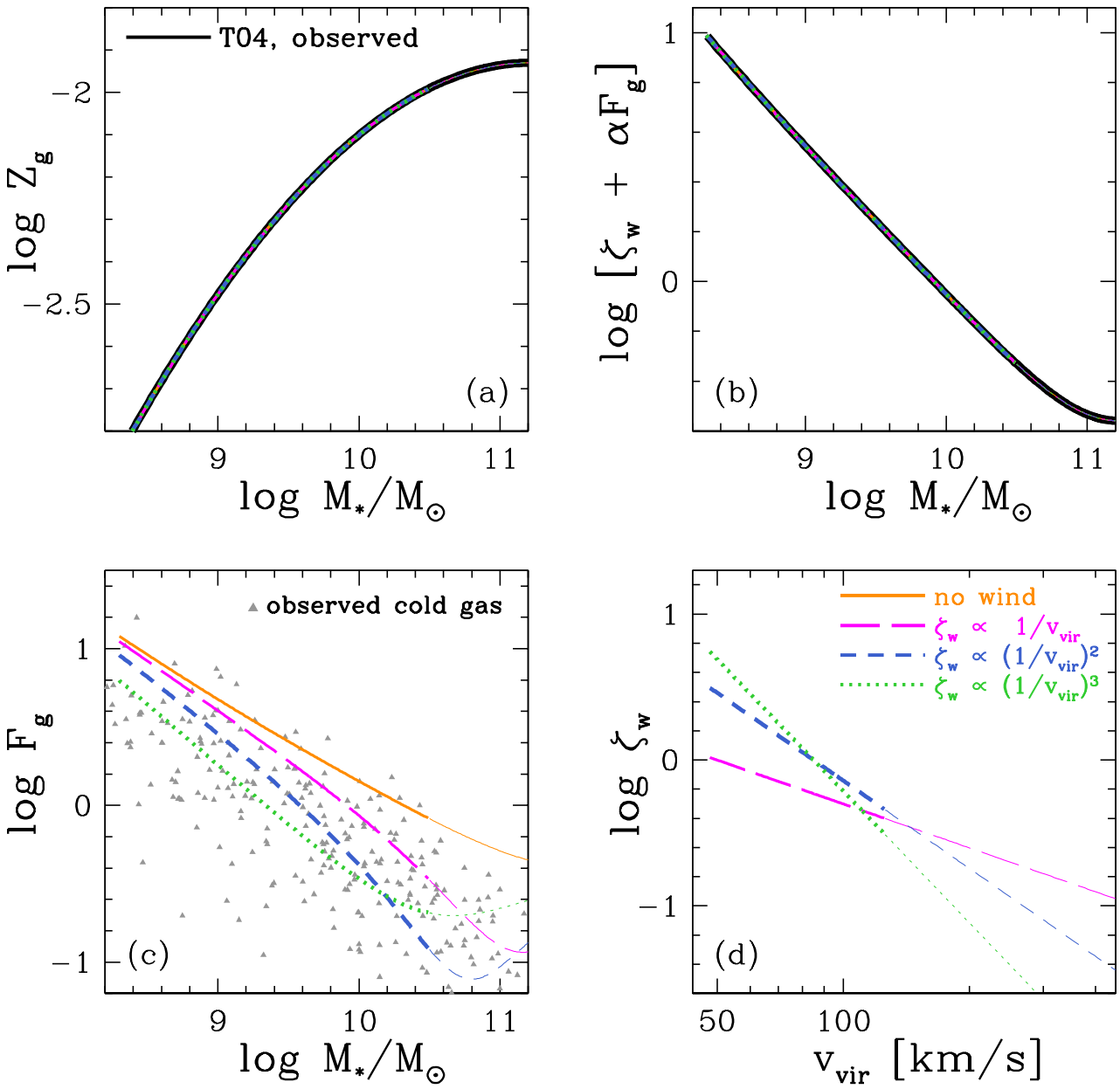

Figure 4. Required gas fractions to reproduce the T04 mass-metallicity relation with varying power-law slopes of $\zeta_{\rm w}(v_{\rm vir})$: $\zeta_{\rm w} = 0$ (orange, solid), $[50\,{\rm km\,s^{-1}}]/v_{\rm vir}$ (pink, long dashed), $([85\,{\rm km\,s^{-1}}]/v_{\rm vir})^2$ (blue, short dashed), $([85\,{\rm km\,s^{-1}}]/v_{\rm vir})^3$ (green, dotted); these normalizations are chosen to give gas fractions that are as compatible with the observations as possible. Note that all models fit data in (a) and (b) by construction: panel (a) shows the T04 mass-metallicity relation (black, solid) and models (colored lines) while panel (b) shows $\log[\zeta_{\rm w} + \alpha F_{\rm g}]$ as a function of stellar mass for the four models (colored lines) and $\log[y/Z_{\rm g} - 1]$ for the T04 mass-metallicity relation in black. Panel (c) shows the model $\log F_{\rm g}$ as a function of stellar mass (colored lines) and the observed gas fractions as grey triangles; these are the same observations plotted in Figure 2 (McGaugh 2005; Leroy et al. 2008; West et al. 2009, 2010). The model $\log \zeta_{\rm w}$ as a function of virial velocity are plotted in panel (d) (the $\zeta_{\rm w} = 0$ case is unplotted because of the logarithmic $\zeta_{\rm w}$ axis).

large constant offset $\zeta_{\rm w,0}$, however, means that the parameterization presented here (see, e.g., Figure 5) cannot be directly interpreted in terms of the simple power-law scalings presented in § 2.3. We also caution that $\zeta_{\rm w} \neq \eta_{\rm w}$, and we explore the consequences of metallicity-weighting the mass-loading parameter below (§ 5).

We note that a crucial step in this analysis is the assignment of virial velocities to stellar masses. For example, Finlator & Davé (2008) found that $\zeta_{\rm w} \propto v_{\rm vir}^{-1}$ was sufficient to reproduce the $z \sim 2.2$ mass-metallicity relation (which does not differ significantly in slope from the shallow relations at $z = 0$). In their simulations, however, $M_\star \propto M_{\rm halo}$, which is a shallower relation than our $M_\star \propto M_{\rm halo}^2$, a slope which Moster et al. (2009) finds to approximately hold to $z \sim 2$ (see their Figure 14). Because $M_{\rm halo} \propto v_{\rm vir}^3$, these differences have extreme consequences for the interpretation of how $\zeta_{\rm w}$ scales with $v_{\rm vir}$.

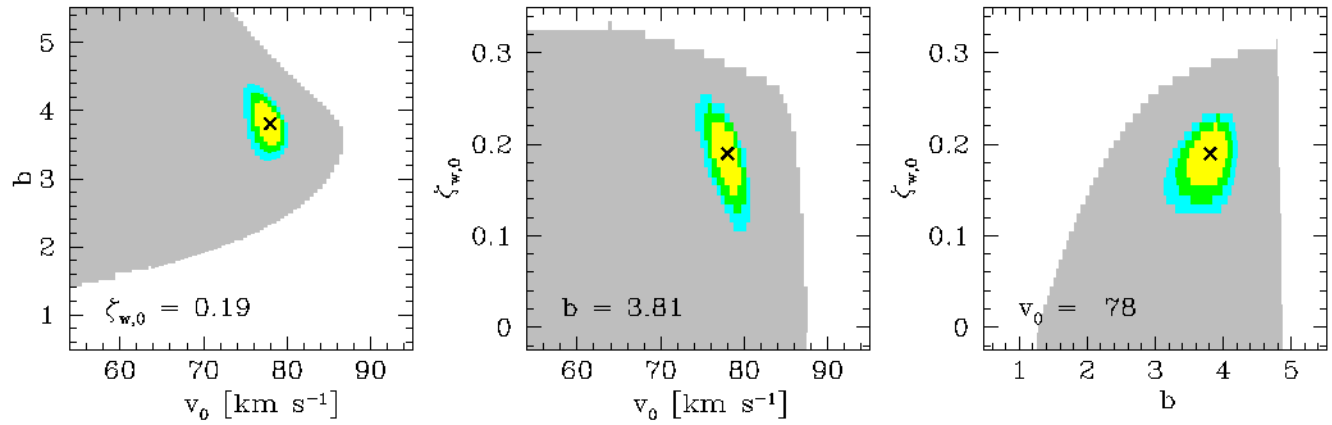

Figure 5. $\Delta\chi^2$ contours for the T04 mass-metallicity relation with $\zeta_{\rm w} = (v_0/v_{\rm vir})^{-b} + \zeta_{\rm w,0}$. The black "X" marks the parameters with the lowest χ^2; the yellow, green, cyan, and grey regions denote solutions with $\Delta\chi^2 \leqslant 1$-σ, 1-$\sigma < \Delta\chi^2 \leqslant 2$-$\sigma$, 2-$\sigma < \Delta\chi^2 \leqslant 3$, and $\Delta\chi^2 > 3$-σ, respectively, using the $\Delta\chi^2$-to-σ conversion from Press et al. (1992). The white regions correspond to unphysical ($M_{\rm g} \leqslant 0$) models.

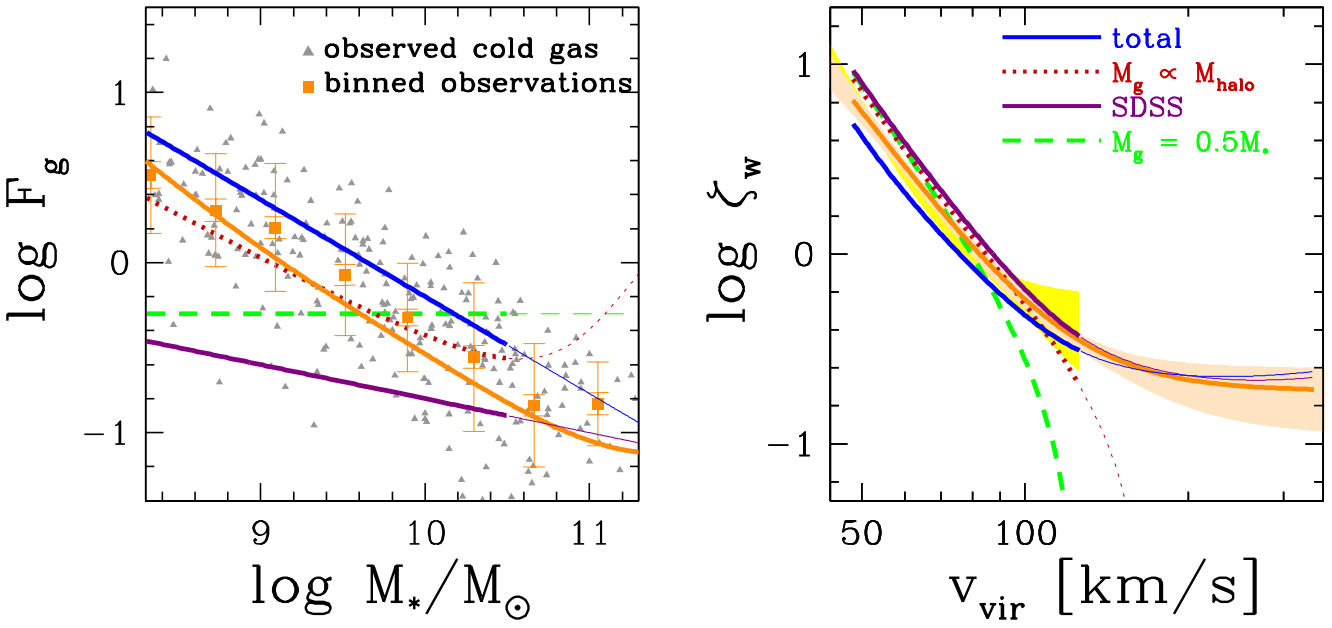

Figure 6. Required $\zeta_{\rm w}$ to reproduce the T04 mass-metallicity relation with varying gas fraction relations: total (blue, solid), $M_{\rm g} = 0.5M_\star$ (green, dashed), inverting the K-S law from SDSS data (purple, solid), and $M_{\rm g} = 0.05(\Omega_b/\Omega_m)M_{\rm halo}$ (red, dotted); see § 2.2 for the motivations behind these relations. *Left*: Gas fractions as a function of stellar mass. The grey triangles in are the gas fractions plotted in Figure 2 (McGaugh 2005; Leroy et al. 2008; West et al. 2009, 2010) and the orange squares are the binned data (§ 2.2). *Right*: $\log \zeta_{\rm w}$ as a function of virial velocity corresponding to the gas fractions in the left panel. The orange lines are the best-fitting models based on the binned data (see Figure 5); the beige and yellow shaded regions in the right-hand panel show the 1-σ range in $\zeta_{\rm w}$ for the entire mass range and $\log M_\star \leqslant 10.5$, respectively.

5 OUTFLOW METALLICITY AND ENTRAINMENT

Supernova-driven galaxy outflows are comprised of some combination of supernova ejecta and ambient interstellar medium entrained in the outflow. The fraction $f_{\rm e}$ of entrained gas determines wind metallicity $Z_{\rm w}$. As mentioned in § 3.1, the wind metallicity $Z_{\rm w}$ is usually assumed to be equal to the ISM metallicity $Z_{\rm g}$ when modeling the mass-metallicity relation, but if the outflowing supernova ejecta entrains very little gas (which would dilute the wind metallicity) then $Z_{\rm w}$ could be much higher than $Z_{\rm g}$.

We showed in § 4 that models of the observed $z = 0$ mass-metallicity relation are more consistent with observations of $z = 0$ galaxy gas fractions when the metallicity-weighted mass-loading factor $\zeta_{\rm w} \equiv (Z_{\rm w}/Z_{\rm g})\eta_{\rm w}$ scales steeply with the halo virial velocity, i.e., $\zeta_{\rm w} = (v_0/v_{\rm vir})^b + \zeta_{\rm w,0}$ with $b \gtrsim 3$. Theoretical models for how supernovae drive galaxy-scale outflows, however, generally predict that the *unweighted* mass-loading factor $\eta_{\rm w} \equiv \dot{M}_{\rm w}/\dot{M}_{\rm SFR} = (\sigma_0/v_{\rm vir})^\beta$ will scale much more shallowly, with $\beta = 1$ or 2 (§ 2.3). Reconciling these disparate scalings therefore requires that $Z_{\rm w}/Z_{\rm g}$ and hence the wind fluid composition varies with galaxy mass.

For any given $\zeta_{\rm w}$ that reproduces the mass-metallicity rela-

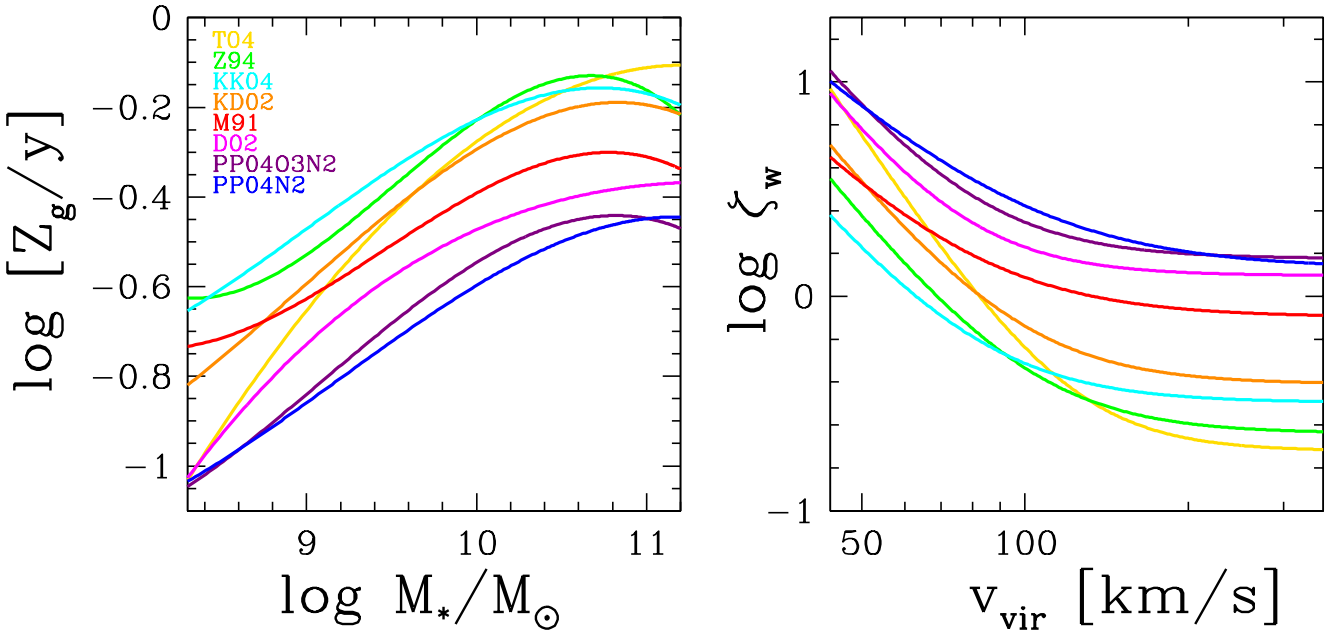

Figure 7. *Left:* The mass-metallicity relation as derived from different metallicity indicators (§ 2.1, Kewley & Ellison 2008), relative to the nucleosynthetic yield $y = 0.015$. *Right:* The corresponding best fitting $\zeta_{\rm w} = (v_0/v_{\rm vir})^b + \zeta_{\rm w,0}$ under the requirement that the models' gas fractions are consistent with observations. The $\zeta_{\rm w}$ parameters are listed in Table 4.

tion, additionally assuming the form of $\eta_{\rm w}(v_{\rm vir})$ uniquely constrains the wind metallicity $Z_{\rm w}(M_\star)$. Figure 9 shows $Z_{\rm w}$ for the best-fit $\zeta_{\rm w} = (78\,{\rm km\,s^{-1}}/v_{\rm vir})^{3.81} + 0.19$ for the T04 mass-metallicity relation (left) and $\zeta_{\rm w} = (79\,{\rm km\,s^{-1}}/v_{\rm vir})^{3.42} + 1.25$ for the D02 mass-metallicity relation (right). The dotted, short-dashed, and long-dashed lines are for $\eta_{\rm w} \propto v_{\rm vir}^{-1}$, $v_{\rm vir}^{-2}$, and $v_{\rm vir}^{-3}$, models, respectively. If $\eta_{\rm w}$ has a similar scaling with mass as $\zeta_{\rm w}$, then $Z_{\rm w} \sim Z_{\rm g}$ for all masses. However, a less steep dependence of $\eta_{\rm w}$ on $v_{\rm vir}$ implies that outflow metallicities should depend less on galaxy mass than $Z_{\rm g}$. Moreover, determining $Z_{\rm w}$ from galaxy wind observations has different systematics than determining $\eta_{\rm w}$, and $Z_{\rm w}$ clearly depends sensitively on the scaling of $\eta_{\rm w}$. Figure 9 shows how measurements of $Z_{\rm w}(M_\star)$ can therefore be used to place unique constraints on $\eta_{\rm w}$.

Physically, different scalings of $\eta_{\rm w}$ and $\zeta_{\rm w}$ (and thus $Z_{\rm g}$ and $Z_{\rm w}$) indicate that the entrainment fraction $f_{\rm e}$ (equation 21) varies with galaxy mass, offering a clue to the physics of galaxy outflows. If, for example, $f_{\rm e}$ increases with increasing gas mass (and thus galaxy mass), it would indicate that the wind fluid does not "punch" through a blanketting column density of gas but instead sweeps up this material and expels it from the galaxy. On the other hand, $f_{\rm e}$ decreasing with increasing galaxy mass, would indicate that the ability of supernova ejecta to collect the surrounding ISM into the wind fluid depends on the depth of the galaxy potential well. We find the former to be the case: to reconcile a steep $\zeta_{\rm w}$ scaling with a shallower $\eta_{\rm w}$ scaling, then winds driven from deeper potential wells must be *more* efficient at entraining the ambient ISM than those driven from shallow potential wells. We also find that in order to have the normalization of $\eta_{\rm w}$ be consistent with the normalizations suggested in § 2.3 (i.e., $v_0 \sim 70\,{\rm km\,s^{-1}}$) then the entrainment fraction must be ~ 1, though the exact value is dependent on the value of $Z_{\rm ej,max}$. This is particularly interesting in light of interpretations of X-ray emitting outflows in which the wind fluid is almost entirely comprised of supernova ejecta, i.e., $f_{\rm e} \sim 0$ (e.g., Strickland & Heckman 2009).

6 SUMMARY AND DISCUSSION

6.1 The approach: modeling a system of galaxies

We present a new formalism in which to understand the mass-metallicity relation. We have shown (§ 3.1 and equation 27) that the gas phase (oxygen) metallicity $Z_{\rm g}$ of star forming galaxies is

$$Z_{\rm g} = y\,[\zeta_{\rm w} - \zeta_{\rm a} + \alpha F_{\rm g} + 1]^{-1}\,, \qquad (35)$$

where y is the nucleosynthetic yield, $\zeta_{\rm a}$ describes accreting metals, $\zeta_{\rm w}$ describes the efficiency of metal expulsion, $F_{\rm g}$ describes dilution by gas, and α is a factor of order unity (see equation 28). In the absence of metal accretion ($\zeta_{\rm a} = 0$), equation (35) shows that the metallicity $Z_{\rm g}$ is set by a balance of outflows ($\zeta_{\rm w}$) and gas dilution ($\alpha F_{\rm g}$), with the normalization set by the nucleosynthetic yield y. This equation represents a general result: each piece can vary with galaxy mass, halo mass, and redshift. To the extent that the star formation history is not bursty, i.e., $\dot{M}_{\rm SFR}$ varies slowly on timescales of 10 Myr (see Appendix A) then the yield y can be taken as constant with time, letting equation (35) describe the instantaneous state of a sequence of galaxies. Galaxies at $z = 0$ are assumed to live on a hypersurface described by their stellar masses, gas fractions, metallicities, outflow and host halo properties. By taking gas fractions and metallicities from observations, we are therefore able to uniquely solve for outflow properties in terms of galaxy masses or metallicities (that are therefore easily comparable to observations) or in terms of the galaxy potential (and therefore easily comparable to models of the underlying wind physics). The only fitting of models to data in this approach is that of functional forms to observations of the mass-metallicity relation (e.g., Kewley & Ellison

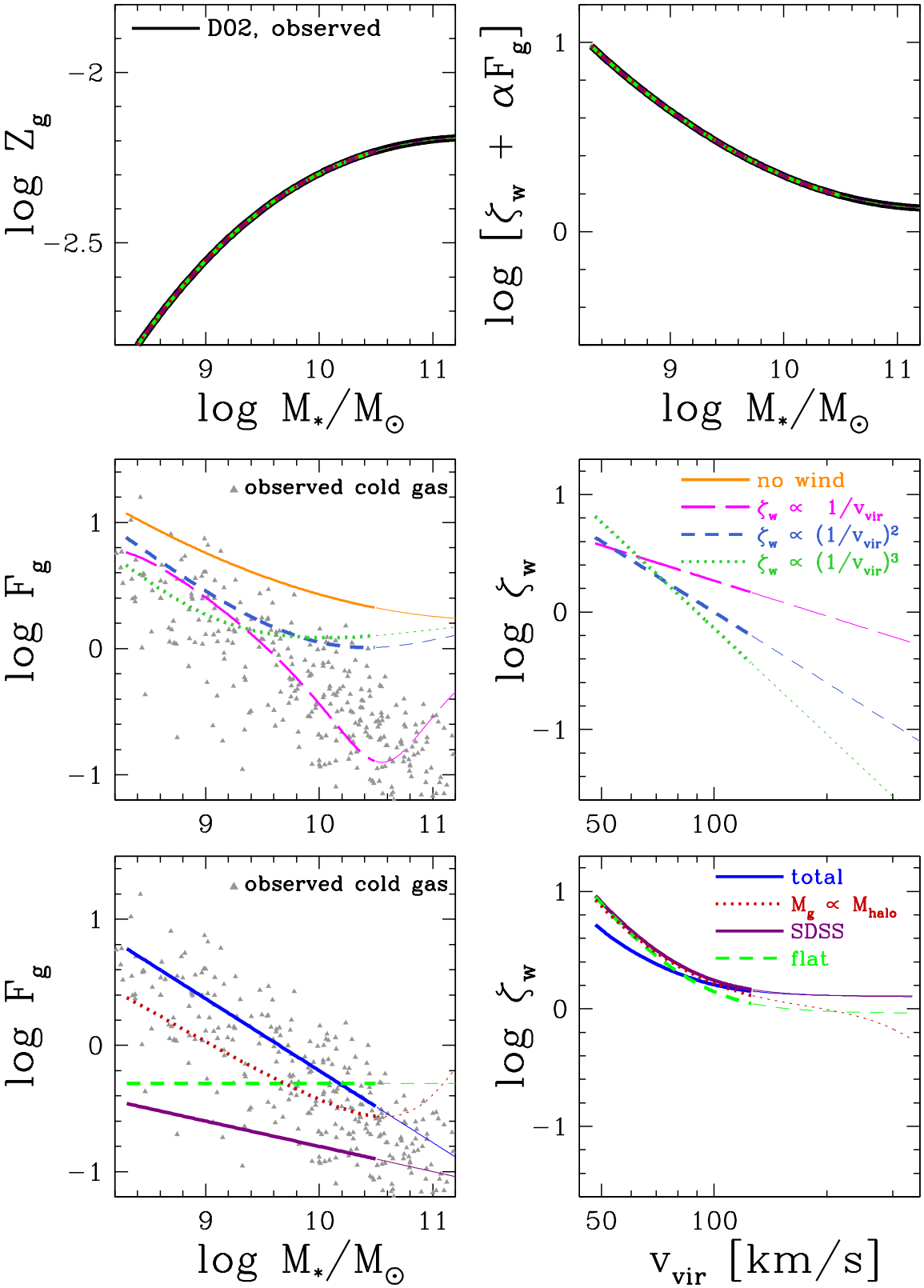

Figure 8. Same as Figures 4 and 6, but for the Denicoló et al. (2002) mass-metallicity relation. The normalizations for $\zeta_{\rm w} \propto v_{\rm vir}^{-b}$ in the middle two panels are chosen to give gas fractions that are as compatible with the observations as possible and are: $[185\,{\rm km\,s^{-1}}]/v_{\rm vir}$ (pink, long dashed), $([100\,{\rm km\,s^{-1}}]/v_{\rm vir})^2$ (blue, short dashed), $([90\,{\rm km\,s^{-1}}]/v_{\rm vir})^3$ (green, dotted).

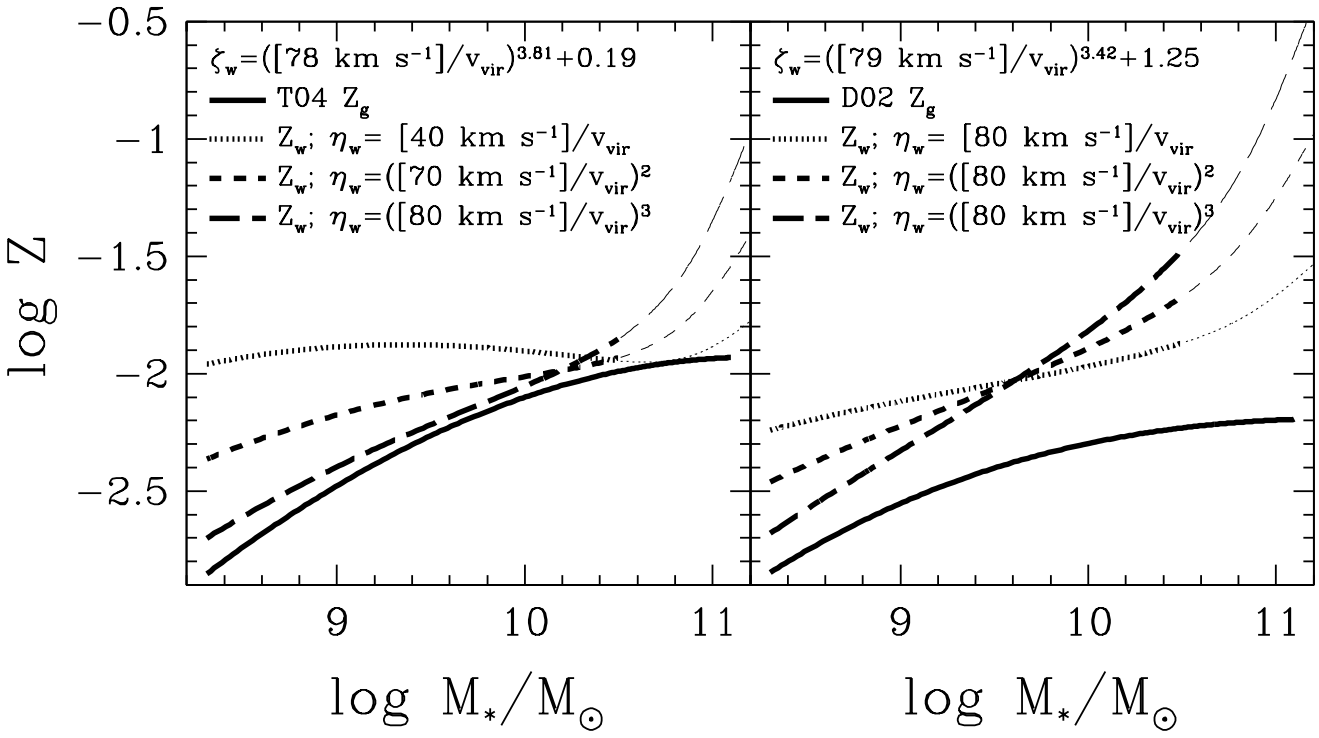

Figure 9. Wind metallicities $Z_{\rm w}$ for the best-fit $\zeta_{\rm w}$ T04 (left) and D02 (right) mass-metallicity relations (see Figures 6 and 8). The solid line corresponds to $\zeta_{\rm w} = \eta_{\rm w}$ and therefore $Z_{\rm w} = Z_{\rm g}$ and $f_{\rm e} = 1$; different scalings for $\eta_{\rm w} = (\sigma_0/v_{\rm vir})^{\beta}$ are shown as the dotted ($\beta = 1$), short-dashed ($\beta = 2$), and long-dashed ($\beta = 3$) lines.

2008) and either models or parameterizations to gas fractions as a function of stellar mass (§ 2.2). Because there is theoretical uncertainty in which metallicity indicator(s) to use when calculating the mass-metallicity relation from data, we do not favor a particular indicator when drawing our conclusions, and specifically state which constraints come from which pieces of the mass-metallicity relation.

6.2 Resulting constraints

We consider implications for both the efficiency of star-formation driven galaxy outflows and for the content of the outflowing material. The two relevant outflow efficiencies are the efficiency with which a galaxy expels its metals, $\zeta_{\rm w} \equiv (Z_{\rm w}/Z_{\rm g})(\dot{M}_{\rm w}/\dot{M}_{\rm SFR})$, which we parameterize as $\zeta_{\rm w} = (v_0/v_{\rm vir})^b + \zeta_{\rm w,0}$. The second relevant efficiency is that with which a galaxy expels its gas, the unweighted mass-loading parameter $\eta_{\rm w} \equiv \dot{M}_{\rm w}/\dot{M}_{\rm SFR}$, which we similarly parameterize as $\eta_{\rm w} = (\sigma_0/v_{\rm vir})^{\beta}$, where β is predicted to be ~ 1 or ~ 2 with $\sigma_0 = 70$–$80\,{\rm km\,s^{-1}}$ (§ 2.3). The content of the wind is observed by its metallicity $Z_{\rm w}$, which can be expressed in terms of the fraction of entrained ISM in the outflow, $f_{\rm e}$, where $Z_{\rm w} = (1 - f_{\rm e})Z_{\rm ej,max} + f_{\rm e}Z_{\rm g}$ (equation 21 in § 3.1). Under the assumptions that $Z_{\rm IGM} = 0$ and y is constant, we draw the following conclusions by requiring that viable models reproduce both the $z = 0$ mass-metallicity relation and are consistent with observed cold gas fractions.

6.2.1 *The necessity of outflows*

Models with no outflows ($\dot{M}_{\rm w} = 0 \Rightarrow \zeta_{\rm w} = 0$) are inconsistent with observed galaxy gas fractions. Specifically, in the absence of winds, the gas masses needed to dilute the produced metals are higher at all galaxy masses than the total observed cold gas masses; the magnitude of this offset is as great as ~ 0.3 dex in $F_{\rm g} \equiv M_{\rm g}/M_{\star}$, depending on the particular mass-metallicity relation being modeled.

6.2.2 *Constraints from the normalization of the mass-metallicity relation*

Equation (35) makes it clear that the nucleosynthetic yield sets the normalization of the mass-metallicity relation. From a modeling perspective, it is useful to consider the mass-metallicity relation normalization relative to the yield (rather than their absolute values) because the true nucleosynthetic yield is unknown to a factor of two due to uncertainties in both the IMF and in Type II supernova physics (Appendix A). Likewise, the overall normalization of the mass-metallicity relation (§ 2.1) is unknown at the ~ 0.3 dex level.[4] The normalization of $y/Z_{\rm g}$ sets the value of the constant offset $\zeta_{\rm w,0} > 0$ (which is set by the turnover of the mass-metallicity relation, see below). The typical required velocity normalization $v_0 \sim 70$–$80\,{\rm km\,s^{-1}}$ is consistent with expectations.

[4] Though neither the nucleosynthetic yield nor the normalization of the mass-metallicity relation are well determined, the scatter in $\log Z_{\rm g}$ at fixed $M_{\star}$ is known to be ± 0.1 dex (Kewley & Ellison 2008). In light of the formalism presented here, this small scatter implies that either the scatter in both $\alpha F_{\rm g}$ and $\zeta_{\rm w}$ are small, or they are highly correlated.

Low normalization mass-metallicity relations require $\zeta_{\rm w} > 1$ for all relevant masses; if the true nucleosynthetic yield is larger than our fiducial value ($y > 0.015$), then the efficiency with which galaxies expel metals will have to be even stronger. Thus if normal quiescently star forming galaxies are not expelling winds with $\zeta_{\rm w} \gg 1$, then the data prefer a low nucleosynthetic yield and a high normalization of the mass-metallicity relation. Furthermore, because the mass-metallicity relation shifts to lower normalizations at higher redshifts, galaxies at these epochs must have either stronger winds or higher gas fractions than their $z = 0$ counterparts.

6.2.3 *Constraints from the morphology of the mass-metallicity relation*

The morphology of the mass-metallicity relation has two main features: the slope below $\sim M^*$ and the turnover at higher masses. The slope of the mass-metallicity relation largely determines how $\zeta_{\rm w}$ scales with galaxy mass, though with some degeneracies with the normalization and constant offset. For small $F_{\rm g}$, as is the case at $z = 0$, $\zeta_{\rm w}$ should scale roughly as $Z_{\rm g}^{-1}$. The power-law scaling of $\zeta_{\rm w}$ with respect to $v_{\rm vir}$ is typically $b \sim 3$. This need for a high and mass-dependent wind efficiency agrees with several other works (e.g., Dekel & Woo 2003; Dutton et al. 2010b; Sawala et al. 2010; Spitoni et al. 2010).

The turnover[5] in the mass-metallicity relation at $\log M_\star \sim 10.5$ may be an observational artifact of the metallicity indicators saturating at high $Z_{\rm g}$ (§ 2.1); however, if oxygen abundances do asymptote to a particular value at high masses, then this behavior can be used to place strong constraints on galaxy outflow properties. Specifically, both the normalization of the mass-metallicity relation relative to the yield and the effects of $v_{\rm vir}$ increasing sharply above $M^* \sim 10^{11}{\rm M}_\odot$ (Figure 3) must be then taken into consideration; moreover, the interplay between these effects can place stronger constraints on viable models than just considerations of the mass-metallicity relation below $10^{10.5}{\rm M}_\odot$. Morphologically, a turnover in the mass-metallicity relation means that either $\alpha F_{\rm g}$ or $\zeta_{\rm w}$ cannot be approximated as a power-law. Because cold gas fractions are observed to roughly follow a power-law with respect to $M_\star$, then $\zeta_{\rm w}$ needs a constant offset $\zeta_{\rm w,0} \sim 0.2$–1.5, depending on which indicator is used to calculate the mass-metallicity relation. We note that, in several cases, if $M_{\rm g} \propto (\Omega_b/\Omega_m)M_{\rm halo}$, then $\zeta_{\rm w}$ can be described as a power-law; physically, this would imply that galaxies above M^* have large reservoirs of ionized gas that are able to efficiently transfer mass with colder, star-forming gas.

If $\zeta_{\rm w}$ and $\eta_{\rm w}$ scale differently with galaxy mass, then the fraction of entrained ISM in the wind fluid will vary with galaxy mass. Observationally this will be seen as $Z_{\rm w}/Z_{\rm g}$ varying with mass. As the morphology of the mass-metallicity relation constrains the scaling of $\zeta_{\rm w}$ with mass, the scaling of $Z_{\rm w}$ and thus $\eta_{\rm w}$ with mass therefore depends on the slope of the mass-metallicity relation. For example (see Figure 9), for a fixed $\eta_{\rm w}$, a steep mass-metallicity relation will lead to a shallower $Z_{\rm w}$-$M_\star$ relation than a shallower mass-metallicity relation will. However, since current uncertainties in the slope of the mass-metallicity relation are smaller than uncertainties in how (or if) $\eta_{\rm w}$ scales with mass, measurements of $Z_{\rm w}$ across a large range in galaxy mass, especially above M^*, will be particularly useful for constraining how $\eta_{\rm w}$ (and $\zeta_{\rm w}$) scale.

[5] The turn-"up" at low masses for the Z94 mass-metallicity relation is unphysical and due to the cubic fit to the data.

6.3 The role of metal-(re)accretion

At $z = 0$, the assumption that accreting material has a negligible metal content (i.e., that $Z_{\rm IGM} = 0$ and therefore $\zeta_{\rm a} = 0$) may not be entirely safe. The IGM is enriched as early as $z > 3$ (Songaila & Cowie 1996; Ellison et al. 2000; Schaye et al. 2003), and if this material is re-accreted onto galaxies at later epochs it could have a significant effect on the shape and normalization of the $z = 0$ mass-metallicity relation. The re-accretion of winds (i.e., gas with $Z_{\rm IGM} > 0$) is a significant component of accreted gas in cosmological SPH simulations (Oppenheimer et al. 2009). Though the total accretion rate scales with halo mass ($\dot{M}_{\rm acc} \propto M_{\rm halo} \propto v_{\rm vir}^3$, see Appendix B), the contribution of accreted metals to the mass-metallicity relation may not scale so steeply (Finlator & Davé 2008). Moreover, an extra source of metals $\zeta_{\rm a}$ will imply that the *amplitude* of outflows $\zeta_{\rm w}$ will need to be even higher than the ones presented here. However, the reaccretion of wind material seen in SPH simulations may be sensitive to numerical issues in the wind implementation; more detailed investigations are needed to verify the importance of wind-recycling. The metal budget available for re-accretion depends on both the amount of metals expelled at higher redshifts and the recyclying timescale. We will address the metal content of winds at $z > 0$ as implied by the evolution of the mass-metallicity relation in a later paper.

ACKNOWLEDGEMENTS

We are indebted to David Weinberg and Todd Thompson for numerous enlightening discussions and comments on the text. We thank Romeel Davé, Rick Pogge, Francesco Calura, Francesca Matteucci, Dušan Kereš, Avi Loeb, and Simon White for useful conversations and Paul Martini, Brett Andrews, and Jonathan Bird for assistance with obtaining and plotting much of the data presented here. We are grateful for Andrew West and Barbara Catinella for providing us with the stellar and gas masses plotted in many of our figures. FS acknowledges support from the Alexander von Humboldt Foundation and partial support from NASA Grant NNG05GH77G.

REFERENCES

Adelman-McCarthy, J. K., et al. 2006, ApJS, 162, 38
Baes, M., Buyle, P., Hau, G. K. T., & Dejonghe, H. 2003, MNRAS, 341, L44
Barkana, R. & Loeb, A. 2001, PhysRep, 349, 125
Bernardi, M., Shankar, F., Hyde, J. B., Mei, S., Marulli, F., & Sheth, R. K. 2010, MNRAS, 436
Boomsma, R., Oosterloo, T. A., Fraternali, F., van der Hulst, J. M., & Sancisi, R. 2008, A&A, 490, 555
Bresolin, F. 2006, ArXiv Astrophysics e-prints
Brinchmann, J., Charlot, S., White, S. D. M., Tremonti, C., Kauffmann, G., Heckman, T., & Brinkmann, J. 2004, MNRAS, 351, 1151
Brooks, A. M., Governato, F., Booth, C. M., Willman, B., Gardner, J. P., Wadsley, J., Stinson, G., & Quinn, T. 2007, ApJL, 655, L17
Bryan, G. L. & Norman, M. L. 1998, ApJ, 495, 80
Calura, F. & Menci, N. 2009, ArXiv e-prints
Calura, F., Pipino, A., Chiappini, C., Matteucci, F., & Maiolino, R. 2009, A&A, 504, 373

Catinella, B., Schiminovich, D., Kauffmann, G., Fabello, S., Wang, J., Hummels, C., Lemonias, J., Moran, S. M., Wu, R., Giovanelli, R., Haynes, M. P., Heckman, T. M., Basu-Zych, A. R., Blanton, M. R., Brinchmann, J., Budavári, T., Gonçalves, T., Johnson, B. D., Kennicutt, R. C., Madore, B. F., Martin, C. D., Rich, M. R., Tacconi, L. J., Thilker, D. A., Wild, V., & Wyder, T. K. 2010, MNRAS, 403, 683
Chabrier, G. 2003a, PASP, 115, 763
—. 2003b, ApJL, 586, L133
Chevalier, R. A. & Clegg, A. W. 1985, Nature, 317, 44
Chieffi, A. & Limongi, M. 2004, ApJ, 608, 405
Conroy, C. & Wechsler, R. H. 2009, ApJ, 696, 620
Crain, R. A., Eke, V. R., Frenk, C. S., Jenkins, A., McCarthy, I. G., Navarro, J. F., & Pearce, F. R. 2007, MNRAS, 377, 41
Dalcanton, J. J. 2007, ApJ, 658, 941
Dekel, A. & Birnboim, Y. 2006, MNRAS, 368, 2
Dekel, A. & Silk, J. 1986, ApJ, 303, 39
Dekel, A. & Woo, J. 2003, MNRAS, 344, 1131
Denicoló, G., Terlevich, R., & Terlevich, E. 2002, MNRAS, 330, 69
Diemand, J., Kuhlen, M., & Madau, P. 2007, ApJ, 667, 859
Dutton, A. A., Conroy, C., van den Bosch, F. C., Prada, F., & More, S. 2010a, ArXiv e-prints
Dutton, A. A., van den Bosch, F. C., & Dekel, A. 2010b, MNRAS, 608
Ellison, S. L., Songaila, A., Schaye, J., & Pettini, M. 2000, AJ, 120, 1175
Erb, D. K. 2008, ApJ, 674, 151
Erb, D. K., Shapley, A. E., Pettini, M., Steidel, C. C., Reddy, N. A., & Adelberger, K. L. 2006a, ApJ, 644, 813
Erb, D. K., Steidel, C. C., Shapley, A. E., Pettini, M., Reddy, N. A., & Adelberger, K. L. 2006b, ApJ, 646, 107
Ferrarese, L. 2002, ApJ, 578, 90
Finlator, K. & Davé, R. 2008, MNRAS, 385, 2181
Firmani, C., Avila-Reese, V., & Rodriguez-Puebla, A. 2009, ArXiv e-prints
Garcia-Appadoo, D. A., West, A. A., Dalcanton, J. J., Cortese, L., & Disney, M. J. 2009, MNRAS, 394, 340
Garnett, D. R. 2002, ApJ, 581, 1019
Genel, S., Genzel, R., Bouché, N., Sternberg, A., Naab, T., Schreiber, N. M. F., Shapiro, K. L., Tacconi, L. J., Lutz, D., Cresci, G., Buschkamp, P., Davies, R. I., & Hicks, E. K. S. 2008, ApJ, 688, 789
Grimes, J. P., Heckman, T., Aloisi, A., Calzetti, D., Leitherer, C., Martin, C. L., Meurer, G., Sembach, K., & Strickland, D. 2009, ApJS, 181, 272
Grimes, J. P., Heckman, T., Hoopes, C., Strickland, D., Aloisi, A., Meurer, G., & Ptak, A. 2006, ApJ, 648, 310
Guo, Q., White, S., Li, C., & Boylan-Kolchin, M. 2009, ArXiv e-prints
Heckman, T. M. 2003, in Revista Mexicana de Astronomia y Astrofisica, vol. 27, Vol. 17, Revista Mexicana de Astronomia y Astrofisica Conference Series, ed. V. Avila-Reese, C. Firmani, C. S. Frenk, & C. Allen, 47–55
Heckman, T. M., Lehnert, M. D., Strickland, D. K., & Armus, L. 2000, ApJS, 129, 493
Hinshaw, G., Weiland, J. L., Hill, R. S., Odegard, N., Larson, D., Bennett, C. L., Dunkley, J., Gold, B., Greason, M. R., Jarosik, N., Komatsu, E., Nolta, M. R., Page, L., Spergel, D. N., Wollack, E., Halpern, M., Kogut, A., Limon, M., Meyer, S. S., Tucker, G. S., & Wright, E. L. 2009, ApJS, 180, 225
Hopkins, P. F., Hernquist, L., Cox, T. J., Dutta, S. N., & Rothberg, B. 2008, ApJ, 679, 156
Kennicutt, Jr., R. C. 1998, ApJ, 498, 541
Kennicutt, Jr., R. C., Bresolin, F., & Garnett, D. R. 2003, ApJ, 591, 801
Kereš, D., Katz, N., Fardal, M., Davé, R., & Weinberg, D. H. 2009, MNRAS, 395, 160
Kereš, D., Katz, N., Weinberg, D. H., & Davé, R. 2005, MNRAS, 363, 2
Kewley, L. J. & Dopita, M. A. 2002, ApJS, 142, 35
Kewley, L. J. & Ellison, S. L. 2008, ApJ, 681, 1183
Kobulnicky, H. A. & Kewley, L. J. 2004, ApJ, 617, 240
Köppen, J., Weidner, C., & Kroupa, P. 2007, MNRAS, 375, 673
Kroupa, P. 2001, MNRAS, 322, 231
Lara-López, M. A., Cepa, J., Bongiovanni, A., Pérez García, A. M., Ederoclite, A., Castañeda, H., Fernández Lorenzo, M., Póvic, M., & Sánchez-Portal, M. 2010, ArXiv e-prints
Leroy, A. K., Walter, F., Brinks, E., Bigiel, F., de Blok, W. J. G., Madore, B., & Thornley, M. D. 2008, AJ, 136, 2782
Loeb, A. & Peebles, P. J. E. 2003, ApJ, 589, 29
Łokas, E. L. & Mamon, G. A. 2001, MNRAS, 321, 155
Mannucci, F., Cresci, G., Maiolino, R., Marconi, A., & Gnerucci, A. 2010, ArXiv e-prints
Martin, C. L. 2005, ApJ, 621, 227
Martin, C. L. & Bouché, N. 2009, ApJ, 703, 1394
Matteucci, F. 2002, ArXiv Astrophysics e-prints
McGaugh, S. S. 1991, ApJ, 380, 140
—. 2005, ApJ, 632, 859
More, S., van den Bosch, F. C., Cacciato, M., Skibba, R., Mo, H. J., & Yang, X. 2010, ArXiv e-prints
Moster, B. P., Somerville, R. S., Maulbetsch, C., van den Bosch, F. C., Maccio', A. V., Naab, T., & Oser, L. 2009, ArXiv e-prints
Murray, N., Quataert, E., & Thompson, T. A. 2005, ApJ, 618, 569
Navarro, J. F., Frenk, C. S., & White, S. D. M. 1996, ApJ, 462, 563
Neistein, E., van den Bosch, F. C., & Dekel, A. 2006, MNRAS, 372, 933
Oppenheimer, B. D., Davé, R., Kereš, D., Fardal, M., Katz, N., Kollmeier, J. A., & Weinberg, D. H. 2009, ArXiv e-prints
Peeples, M. S., Pogge, R. W., & Stanek, K. Z. 2008, ApJ, 685, 904
—. 2009, ApJ, 695, 259
Pettini, M. & Pagel, B. E. J. 2004, MNRAS, 348, L59
Pizagno, J., Prada, F., Weinberg, D. H., Rix, H., Pogge, R. W., Grebel, E. K., Harbeck, D., Blanton, M., Brinkmann, J., & Gunn, J. E. 2007, AJ, 134, 945
Portinari, L., Chiosi, C., & Bressan, A. 1998, A&A, 334, 505
Press, W. H., Teukolsky, S. A., Vetterling, W. T., & Flannery, B. P. 1992, Numerical Recipes in C (Cambridge University Press: Cambridge)
Recchi, S., Calura, F., & Kroupa, P. 2009, A&A, 499, 711
Rupke, D. S., Veilleux, S., & Sanders, D. B. 2002, ApJ, 570, 588
Salpeter, E. E. 1955, ApJ, 121, 161
Salucci, P., Lapi, A., Tonini, C., Gentile, G., Yegorova, I., & Klein, U. 2007, MNRAS, 378, 41
Samui, S., Subramanian, K., & Srianand, R. 2008, MNRAS, 385, 783
Sawala, T., Scannapieco, C., Maio, U., & White, S. 2010, MNRAS, 402, 1599
Schaye, J., Aguirre, A., Kim, T., Theuns, T., Rauch, M., & Sargent, W. L. W. 2003, ApJ, 596, 768
Schiminovich, D., Catinella, B., Kauffmann, G., Fabello, S., Wang, J., Hummels, C., Lemonias, J., Moran, S. M., Wu, R.,

Giovanelli, R., Haynes, M. P., Heckman, T. M., Basu-Zych, A. R., Blanton, M. R., Brinchmann, J., Budavari, T., Goncalves, T., Johnson, B. D., Kennicutt, R. C., Madore, B. F., Martin, C. D., Rich, M. R., Tacconi, L. J., Thilker, D. A., Wild, V., & Wyder, T. K. 2010, ArXiv e-prints
Schmidt, M. 1959, ApJ, 129, 243
Searle, L. & Sargent, W. L. W. 1972, ApJ, 173, 25
Shankar, F., Lapi, A., Salucci, P., De Zotti, G., & Danese, L. 2006, ApJ, 643, 14
Silk, J. & Rees, M. J. 1998, A&A, 331, L1
Socrates, A., Davis, S. W., & Ramirez-Ruiz, E. 2008, ApJ, 687, 202
Songaila, A. & Cowie, L. L. 1996, AJ, 112, 335
Spitoni, E., Calura, F., Matteucci, F., & Recchi, S. 2010, ArXiv e-prints
Spoon, H. W. W. & Holt, J. 2009, ApJL, 702, L42
Springel, V. 2005, MNRAS, 364, 1105
Strickland, D. K. & Heckman, T. M. 2007, ApJ, 658, 258
—. 2009, ApJ, 697, 2030
Strickland, D. K. & Stevens, I. R. 2000, MNRAS, 314, 511
Tonini, C., Lapi, A., Shankar, F., & Salucci, P. 2006, ApJL, 638, L13
Tremonti, C. A., Heckman, T. M., Kauffmann, G., Brinchmann, J., Charlot, S., White, S. D. M., Seibert, M., Peng, E. W., Schlegel, D. J., Uomoto, A., Fukugita, M., & Brinkmann, J. 2004, ApJ, 613, 898
Tully, R. B. & Fisher, J. R. 1977, A&A, 54, 661
Vale, A. & Ostriker, J. P. 2004, MNRAS, 353, 189
Veilleux, S., Cecil, G., & Bland-Hawthorn, J. 2005, ARA&A, 43, 769
Wadsley, J. W., Stadel, J., & Quinn, T. 2004, New Astronomy, 9, 137
Wallerstein, G. 1962, ApJS, 6, 407
Walter, F., Brinks, E., de Blok, W. J. G., Bigiel, F., Kennicutt, R. C., Thornley, M. D., & Leroy, A. 2008, AJ, 136, 2563
West, A. A., Garcia-Appadoo, D. A., Dalcanton, J. J., Disney, M. J., Rockosi, C. M., & Ivezić, Ž. 2009, AJ, 138, 796
West, A. A., Garcia-Appadoo, D. A., Dalcanton, J. J., Disney, M. J., Rockosi, C. M., Ivezić, Ž., Bentz, M. C., & Brinkmann, J. 2010, AJ, 139, 315
Woosley, S. E. & Weaver, T. A. 1995, ApJS, 101, 181
Wyse, R. F. G. & Silk, J. 1985, ApJL, 296, L1
Zaritsky, D., Kennicutt, Jr., R. C., & Huchra, J. P. 1994, ApJ, 420, 87

APPENDIX A: THE NUCLEOSYNTHETIC YIELD AND INSTANTANEOUS RECYCLED FRACTION

As shown in Equation (18), the nucleosynthetic yield is

$$y = \frac{\dot{M}_{\rm new\ metals}}{\dot{M}_{\rm recy}} \frac{\dot{M}_{\rm recy}}{\dot{M}_{\rm SFR}} = \frac{\dot{M}_{\rm new\ metals}}{\dot{M}_{\rm SFR}}, \tag{A1}$$

where $\dot{M}_{\rm new\ metals}$ is the rate of metal (i.e., oxygen) production from Type II supernovae and $\dot{M}_{\rm SFR}$ is the current star formation rate. Though $\dot{M}_{\rm recy}$ depends on the star formation history (i.e., the number of old stars), the yield only depends on the star formation history over the previous $\sim 10^7$ years, i.e., the lifetime of stars that produce oxygen. We show in Figure A1 how y varies in time for different choices of star formation history, IMF, and metallicity based on the "B" series Type II supernovae yields from Woosley & Weaver (1995). The Chabrier (2003b) IMF is shown in red and blue, and the Kroupa (2001) IMF is shown in orange and green; both are integrated from 0.08 to $100{\rm M}_\odot$. We apply the Woosley & Weaver supernova yields to bins of stellar mass that match at the midpoints between the model masses; we extrapolate the $40{\rm M}_\odot$ models to $100{\rm M}_\odot$. The effects of metallicity ($Z = Z_\odot$, red and orange; $Z = 0.1Z_\odot$, blue and green) are subdominant to the effects of the IMF. Different line types represent different star formation rates as a function of time, as denoted in the top-left panel. We take stellar lifetimes to be the main sequence lifetime, $\tau_{\rm MS} = \tau_\odot (m/{\rm M}_\odot)^{-\beta} = (10^{10}\ {\rm yr})(m/{\rm M}_\odot)^{-2.5}$, where m is the mass of the star. At the end of its lifetime, a star returns a gas mass of $m - m_{\rm remnant}$ to the ISM, where $m_{\rm remnant} = m_{\rm ns} = 2.0{\rm M}_\odot$ for $8 > m > 11{\rm M}_\odot$ and $m_{\rm remnant} = m_{\rm wd} = 0.6{\rm M}_\odot$ for $m < 8{\rm M}_\odot$; for stars more massive than $11{\rm M}_\odot$, we take the ejected mass to be that calculated by Woosley & Weaver (1995). All recycled mass is taken to be from stars that have been formed since $t = 0$, i.e., we assume that there are no stars at $t = 0$ that will eject mass into the ISM. This analysis implicitly assumes that all gas is well-mixed at all times. The sharp features in the top-right and the bottom two panels are due to our simple stellar evolution model. The feature at $\sim 10^6$ yr arises from the lifetime of $40{\rm M}_\odot$ stars; stars with $m > 40{\rm M}_\odot$ are assumed to have the same yields as $40{\rm M}_\odot$ stars. The feature at $\sim 2.5 \times 10^7$ yr is caused by the lifetime of $11{\rm M}_\odot$ stars: stars with $m < 11{\rm M}_\odot$ are assumed to not explode as Type II supernovae and thus not produce oxygen. (Also, $m = 11{\rm M}_\odot$ is the mass boundary where the remnant mass is taken to be $m_{\rm ns}$ instead of being calculated by Woosley & Weaver.)

The top-right panel of Figure A1 shows the instantaneous (oxygen) metallicity of ejected gas, $Z_{\rm ej}$; this decreases with time because stars with $m < 11{\rm M}_\odot$ do not produce oxygen but still recycle gas to the ISM. The decrease in $Z_{\rm ej}$ before 2.5×10^7 yr reflects the fact higher mass stars produce relatively more oxygen than low-mass stars. We take $Z_{\rm ej,max} = 0.15$, though considering the contribution of all Type II supernovae, $Z_{\rm ej,max}$ could plausibly be in the range 0.1–0.2. The instantaneous recycled gas fraction, $f_{\rm recy}$, is plotted in the bottom-left panel. Though $f_{\rm recy}$ varies continuously with time, its change is slight, and depends strongly on the IMF, slightly on the star formation history, and negligibly on the metallicity. We therefore take $f_{\rm recy} = 0.2$ in our models; varying this between 0.1 and 0.4 has a negligble impact on our results, especially compared to the theoretical uncertainties in $12 + \log({\rm O/H})$ and the nucleosynthetic yield. The nucleosynthetic yield, y, is shown in the bottom-right panel of Figure A1. The strong variations with time seen with both $Z_{\rm ej}$ and $f_{\rm recy}$ are largely gone due to the cancellation of $\dot{M}_{\rm ejecta}$. Since the production of oxygen only lags the star formation rate by $\lesssim 2.5 \times 10^7$ yr, the yield is effectively constant after the initial generation of Type II supernovae explode; if the star formation rate varies strongly over this timescale (e.g., the dotted and short-dashed lines), then a slight deviation in y can be seen. However, even in these extreme circumstances, the dependence on y for $t \gtrsim 2.5 \times 10^7$ yr is small compared to the uncertainties from the IMF. On the other hand, if the star formation history is extremely bursty (e.g., varying by several orders of magnitude) on the scales of 10 Myr (not plotted for clarity), then the instantaneous $\dot{M}_{\rm new\ oxygen}$ and $\dot{M}_{\rm SFR}$ will *not* closely track one another; a galaxy with such a pathological star formation history could develop an observed $Z_{\rm g}$ that is much higher than what is generically understood to be the nucleosynthetic yield.

In a similar calculation, Finlator & Davé (2008) let both the IMF (Salpeter 1955 and Chabrier 2003b) and the Type II supernova yields (Woosley & Weaver 1995; Chieffi & Limongi 2004;

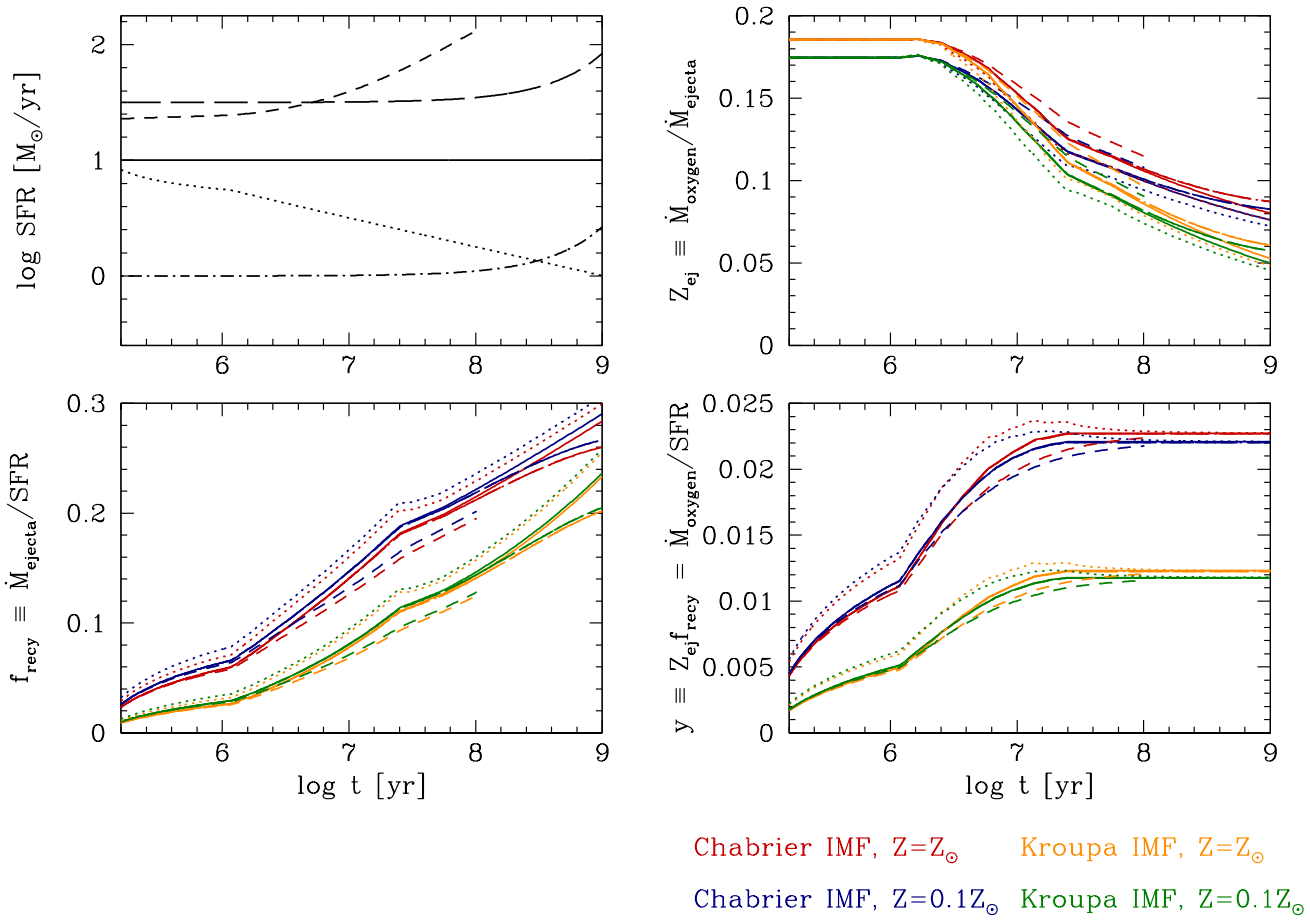

Figure A1. Nucleosynthetic yields y (bottom-right), $Z_{\rm ej}$ (top-right), and instantaneous recycled fractions $f_{\rm recy}$ (bottom-left) as a function of time for different star formation histories (line type, upper-left panel), IMFs (Chabrier 2003a,b, red and blue; Kroupa 2001, orange and green), and metallicities (blue and green, $Z = 0.1Z_\odot$; red and orange, $Z = Z_\odot$).

Portinari et al. 1998) vary; they found that uncertainties in the models allow for $0.008 < y < 0.021$. We adopt $y = 0.015$, which is in the middle of the range given by Finlator & Davé. This yield is somewhat lower than found for Woosley & Weaver models for the Chabrier IMF (our adopted IMF), but we find that larger values of y are more difficult to reconcile with the observed gas fractions (§ 4).

The nucleosynthetic yield y is more commonly seen expressed in terms of a "closed box" model (Searle & Sargent 1972; Matteucci 2002; Tremonti et al. 2004; Dalcanton 2007). In the closed box model, the total mass of the system, $M_{\rm tot} = M_{\rm g} + M_\star$, is a constant; thus, the gas fraction decreases as the stellar mass increases. If instantaneous recycling is also assumed, then as the gas fraction decreases, the metallicity increases according to

$$Z_{\rm g} = y \ln(1/\mu_{\rm g}), \tag{A2}$$

which to first order and for large $F_{\rm g}$, is equivalent to equation (27) with $\zeta_{\rm w} = \zeta_{\rm a} = 0$ and $\alpha = 1$.

Finally, we note that the maximum $Z_{\rm g}$ reached for the Kewley & Ellison mass-metallicity relations (Figure 1) ranges from 0.002 to 0.012. A comparison between $\max(Z_{\rm g})$ and y might be able to set interesting constraints on either the nucleosynthetic yield y (specifically, the Type II supernova yields, modulo the IMF) or on the overall normalization of the mass-metallicity relation as given by different $12 + \log({\rm O/H})$ indicators (see § 2.1). This implies that, e.g., the Tremonti et al. (2004) mass-metallicity relation is inconsistent with models for which $y < 0.012$. More generally, a generic massive galaxy with a low gas fraction and a deep potential well (and thus plausibly ineffective winds) is expected to have a metallicity $Z_{\rm g}$ that approaches y; if by $z = 0$ this is indeed generically the case, then such an analysis would favor smaller values of y and higher normalizations of $12 + \log({\rm O/H})$.

APPENDIX B: OUTFLOWS, INFLOWS, AND STAR FORMATION: GETTING THE GAS MASSES

As shown in § 3.1,

$$\dot{M}_{\rm g} = \dot{M}_{\rm acc} - \dot{M}_{\rm SFR} + \dot{M}_{\rm recy} - \dot{M}_{\rm w} \tag{B1}$$

$$= \dot{M}_{\rm SFR}(\eta_{\rm a} - 1 + f_{\rm recy} - \eta_{\rm w}), \tag{B2}$$

and

$$\frac{{\rm d}M_{\rm g}}{{\rm d}M_\star} = \frac{\eta_{\rm a} - \eta_{\rm w} - 1 + f_{\rm recy}}{1 - f_{\rm recy}} = F_{\rm g}(1 - \gamma). \tag{B3}$$

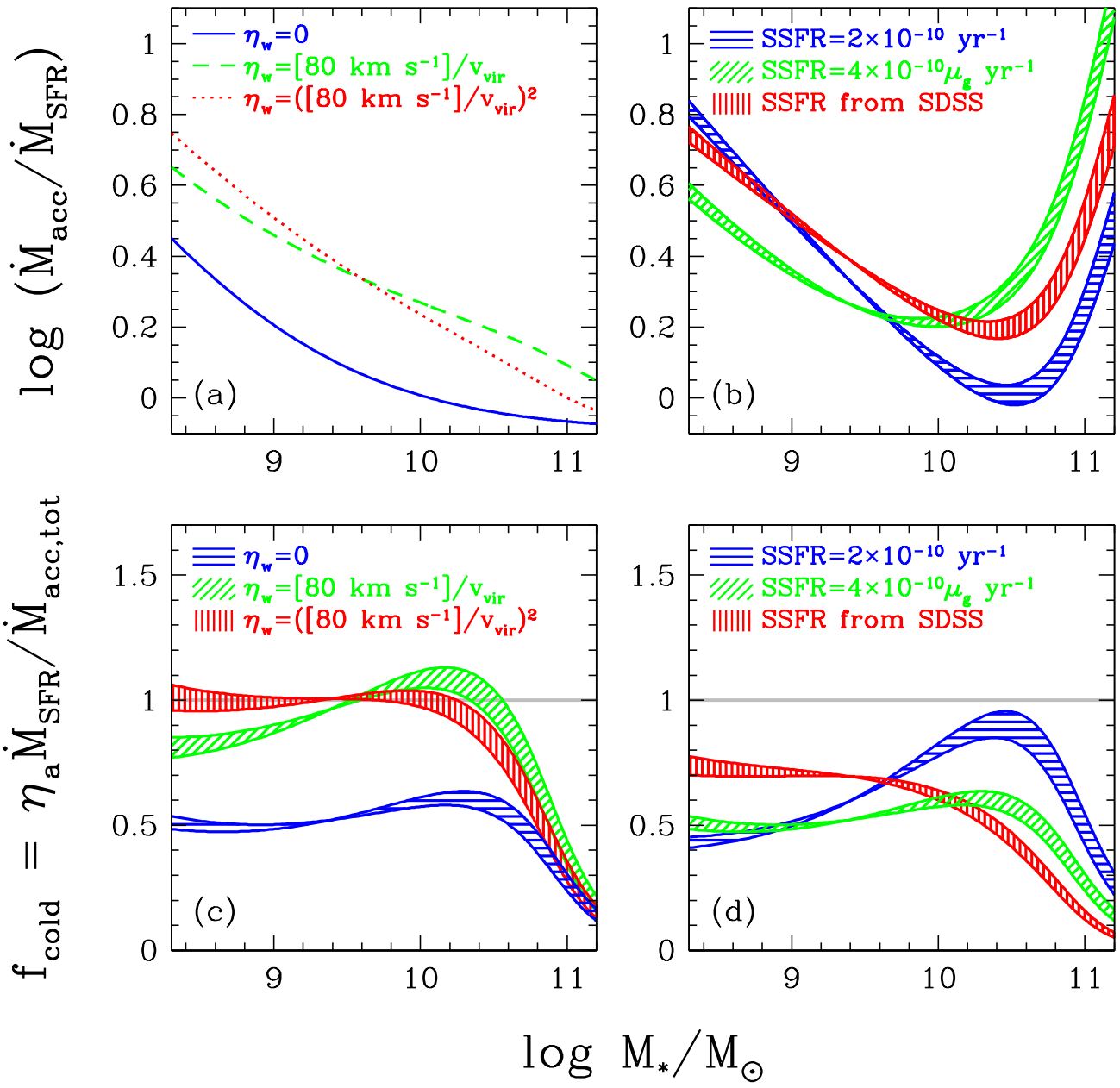

Figure B1. Gas accretion rates, star formation rates, and cold gas accretion fractions as a function of stellar mass with varying outflows and specific star formation rates. All panels assume the total cold gas fractions described in § 2.2. Panel (a) shows how $\eta_{\rm a}$ varies according to equation (B4) for different $\eta_{\rm w}$ models: no wind (solid blue), a momentum-driven scaling (green dashed), and an energy-driven scaling (red dotted). In all cases, high mass galaxies accrete less gas per unit star formation than less massive galaxies. Panel (b) shows the expected range in $\dot{M}_{\rm acc,\,tot}/\dot{M}_{\rm SFR}$ between the Neistein et al. (2006) and Genel et al. (2008) $\dot{M}_{\rm acc}$ models (shaded regions) and with three scalings of $\dot{M}_{\rm SFR}/M_\star$ with stellar mass: constant (blue), $\propto \mu_{\rm g}$ (green), and the median values from SDSS (red). These $\dot{M}_{\rm acc,\,tot}/\dot{M}_{\rm SFR}$ are qualitatively similar at low masses to the $\eta_{\rm a}$ shown in panel (a), but increase rapidly at high masses. Panels (c) and (d) show the ratio $f_{\rm cold}$ of these two estimates, with varying $\eta_{\rm w}$ and the SDSS SSFRs and with varying the SSFR and no winds, respectively.

In § 4 we assumed an $F_{\rm g}$-$M_\star$ relation existed and that as galaxies evolve they remain on such a relation. Here we consider, for a given $\eta_{\rm w}$, what implications such a relation has on the gas accretion rate and how efficiently galaxies are able to turn this accreted gas into stars. The above equations imply that the gas inflow and outflow rates must be balanced by

$$\eta_{\rm a} - \eta_{\rm w} = (1 - f_{\rm recy})F_{\rm g}(1-\gamma) - f_{\rm recy} + 1. \quad \text{(B4)}$$

Thus, for a given combination of $\eta_{\rm w}$ and $F_{\rm g}$, we can uniquely determine $\eta_{\rm a} \equiv \dot{M}_{\rm acc}/\dot{M}_{\rm SFR}$, i.e., the efficiency with which a galaxy turns its accreted gas into stars. For example, if the star formation rate is higher than the accretion rate ($\log \eta_{\rm a} < 0$), then the galaxy is forming stars more quickly than it is accreting gas, i.e. it is very efficient at forming stars. We plot $\log \eta_{\rm a}$ for the no wind, $\eta_{\rm w} = [70\,{\rm km\,s^{-1}}]/v_{\rm vir}$, and $\eta_{\rm w} = ([70\,{\rm km\,s^{-1}}]/v_{\rm vir})^2$ cases as a function of stellar mass in the upper-left panel of Figure B1 for the

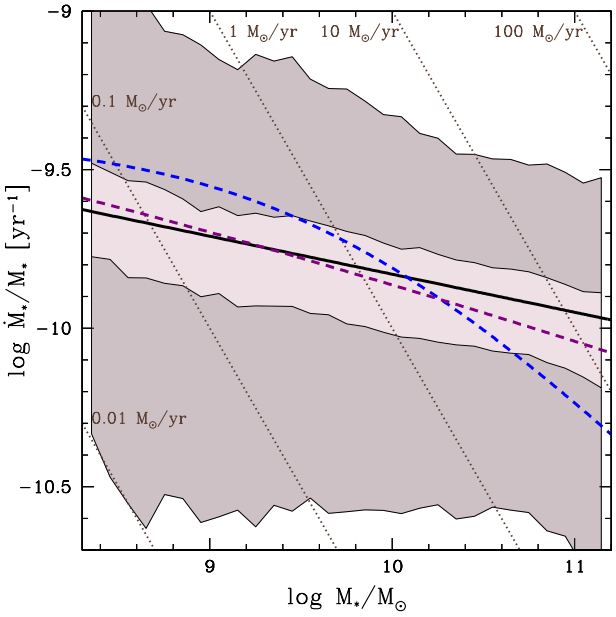

Figure B2. Specific star formation rates. The shaded regions 1- and 2-σ dispersions in running bins of $\log M_\star$ of the aperture-corrected specific star formation rates from SDSS (Brinchmann et al. 2004); the black solid line is a power-law fit to median (equation B5). The purple dashed is the SDSS $\mu_{\rm g} \times 1 \times 10^{-9}$ yr and blue dashed line is the total $\mu_{\rm g} \times 4 \times 10^{-10}$ yr; these offsets imply a star formation timescale of 1–2.5 Gyr. The shaded regions are dotted lines are constant $\dot{M}_{\rm SFR}$.

total gas fraction relation (see Table 3 and Figure 2). Strikingly, $\eta_{\rm a}$ always decreases significantly with increasing mass—even in the absence of winds (solid blue line). This behavior follows directly from the steepness of the gas fraction relation (equation B4). When outflows that preferentially remove gas from low-mass galaxies ($\eta_{\rm w} \propto v_{\rm vir}^{-1}$, green dashed line; $v_{\rm vir}^{-2}$, red dotted line) are taken into account, $\eta_{\rm a}$ likewise increases and steepens to compensate. Therefore, while winds may affect how star-formation efficiency varies as a function of galaxy mass, they are not necessary to explain the trend, implying that additional physics is at play.

This analysis does not entirely reveal what drives the $\eta_{\rm a}$-$M_\star$ relation. However, the nature of $\eta_{\rm a}$ can be unraveled by appealing to $\dot{M}_{\rm SFR}$ and $\dot{M}_{\rm acc}$ from independent sources. For example, as shown in Figure B2, the median specific star formation rate (SSFR, $\dot{M}_{\rm SFR}/M_\star$) in SDSS DR4 star-forming galaxies decreases with increasing $M_\star$, though there is large scatter in the SSFR at fixed $M_\star$. We consider here three scalings for how the SSFR may vary with $M_\star$. The median SSFR of SDSS DR4 star-forming galaxies can be fit with a power law

$$\mathrm{med}(\log[\dot{M}_{\rm SFR}/M_\star]) \approx -9.83 - 0.12(\log[M_\star/{\rm M}_\odot] - 10), \quad \text{(B5)}$$

as shown as a histogram in Figure 10 of Peeples et al. (2009) and the black solid line in Figure B2. A physically-motivated way to have the SSFR to decrease with mass is to postulate that it is proportional to the total gas fraction, $\mu_{\rm g}$. The blue dashed line shows $\mu_{\rm g} \times 4 \times 10^{-10}$ yr for the total gas fractions, while the purple dashed line shows $\mu_{\rm g} \times 1 \times 10^{-9}$ yr for the SDSS gas fractions (note that the SDSS gas fractions were derived largely from these same $\dot{M}_{\rm SFR}$ and thus this is a somewhat degenerate comparison). Finally, we consider a constant SSFR, $\dot{M}_{\rm SFR}/M_\star = 2 \times 10^{-10}$ yr ($\log[\dot{M}_{\rm SFR}/M_\star] = -9.7$ in Figure B2).

Using extended Press-Schechter theory, Neistein et al. (2006) parameterize the baryonic accretion rate onto halos by

$$\dot{M}_{\rm acc,\,tot} = 7.23 \left(\frac{M_{\rm halo}}{10^{12}{\rm M}_\odot}\right)^{1.15} \left(\frac{f_b}{0.181}\right) (1+z)^{2.25}\,{\rm M}_\odot\,{\rm yr}^{-1}, \quad \text{(B6)}$$

where $f_b \equiv \Omega_b/\Omega_m$. Genel et al. (2008) find a similar accretion rate of dark matter onto halos in the Millineum Simulation, which implies a baryonic accretion rate of

$$\dot{M}_{\rm acc,\,tot} = 6.34 \left(\frac{M_{\rm halo}}{10^{12}{\rm M}_\odot}\right)^{1.07} \left(\frac{f_b}{0.181}\right) (1+z)^{2.2}\,{\rm M}_\odot\,{\rm yr}^{-1}. \quad \text{(B7)}$$

These accretion rates are for matter being accreted into the *halo*, not the galaxy, and can be safely considered as upper limits to $\dot{M}_{\rm acc}$.

The range of $\dot{M}_{\rm acc,\,tot}/\dot{M}_{\rm SFR}$ allowed between these two $\dot{M}_{\rm acc}$ models and three SSFRs (constant, solid; $\propto \mu_{\rm g}$, dashed; SDSS median, dotted) are plotted in the top-right panel of Figure B1. At low stellar masses, $M_\star \propto M_{\rm halo}^{0.5}$ (equation 31 and Figure 3), which when combined with the nearly linear mass-dependence of the accretion rate with halo mass, provides $\dot{M}_{\rm acc}/\dot{M}_{\rm SFR} \sim M_{\rm halo}/M_\star \sim M_\star^{-0.5}$, which is the appoximate trend found at $M_\star \lesssim 10^{10}{\rm M}_\odot$. Equations (B6) and (B7) state that the overall "efficiency" of mass accretion $\dot{M}_{\rm acc}/M_{\rm halo}$ is roughly constant with halo mass. Therefore, although the host halos of lower mass galaxies accrete a proportionally equal baryon mass, they are less capable at converting this gas into stars. At high masses, however, the opposite is true: galaxies become more efficient at converting accreted gas into stars. For $M_\star \gtrsim 10^{10}{\rm M}_\odot$, $M_\star \propto M_{\rm halo}^{0.5}$ (equation 31), implying $\dot{M}_{\rm acc}/\dot{M}_{\rm SFR} \sim M_{\rm halo}/M_\star \sim M_\star$, which is close to the observed $\eta_{\rm a}$-$M_\star$ slope at high masses. This combined double mass-dependent behaviour of $\eta_{\rm a}$ with stellar mass produces the characteristic "U" shape observed in Figure B1.

The Neistein et al. and Genel et al. estimates of $\dot{M}_{\rm acc,\,tot}$ are for baryonic accretion into the halo. However, only a fraction of this infalling gas may be usable for star formation; for example, if this onfalling gas is shock-heated as it is accreted, then it will neither be detected in H I+H_2 observations nor contribute towards star formation (since we are sensitive to $\eta_{\rm a}$ rather than $\dot{M}_{\rm acc,\,tot}$ proper, the gas participating in star formation is relevant). Therefore, to better characterize the fraction of gas that is accreted "cold"—and therefore able to further cool and form stars—we combine the estimates of $\dot{M}_{\rm acc}$, $\dot{M}_{\rm SFR}$, and $\eta_{\rm a}$, defining this cold fraction as

$$f_{\rm cold} \equiv \eta_{\rm a} \frac{\dot{M}_{\rm SFR}}{\dot{M}_{\rm acc,\,tot}}, \quad \text{(B8)}$$

where $\dot{M}_{\rm acc,\,tot}$ and $\dot{M}_{\rm SFR}$ are generally defined. For illustrative purposes, we let $\dot{M}_{\rm acc,\,tot}$ be defined as in equations (B6) and (B7). Note that to be physical, $0 \leqslant f_{\rm cold} \leqslant 1$. The lower-left panel of Figure B1 shows how $f_{\rm cold}$ varies with different $\eta_{\rm w}$ scalings, assuming the median SDSS SSFRs, while the lower-right panel shows how $f_{\rm cold}$ depends on the SSFR in the absence of winds.

There are several interesting behaviors in the lower panels of Figure B1 worth noting. First, the morphology of $f_{\rm cold}(M_\star)$ is fairly robust against variations in the SSFR and $\eta_{\rm w}$: it is roughly constant, perhaps with a slight rise, for $\log M_\star \lesssim 10.5$, i.e., below about M^*, and then drops precipitously at higher masses. Physically, this is a restatement of galaxies with masses near M^* being more efficient at turning gas accreted by their halos into stars, relative to either more or less massive galaxies (Shankar et al. 2006; Guo et al. 2009).

Second, $f_{\rm cold}(M_\star) \sim 1$ for low-mass galaxies. At face value, this would imply that all the accreting gas is available for star for-

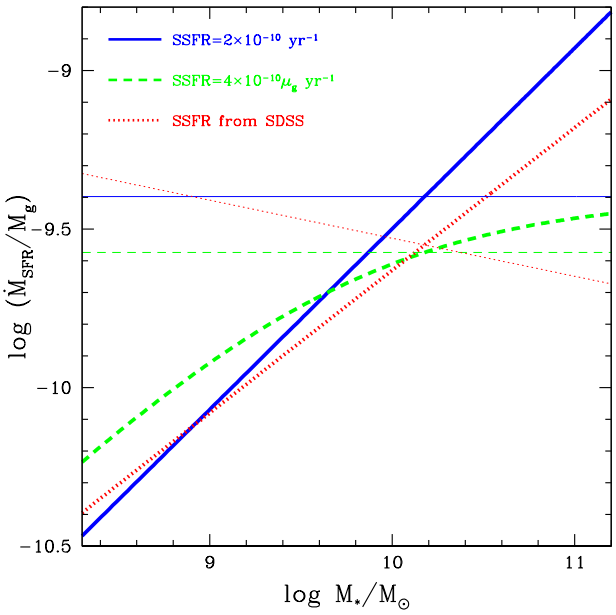

Figure B3. Star formation efficiency $\dot{M}_{\rm SFR}/M_{\rm g}$ as a function of $M_\star$, taking $M_{\rm g}$ to be the total cold gas masses (thick lines, § 2.2) and $M_{\rm g} = 0.5M_\star$ (thin lines) and three choices of the specific star formation rate: constant (solid blue lines), $\propto \mu_{\rm g}$ (dashed green lines), and the median values from SDSS (dotted red lines). In all cases, a steeply decreasing $F_{\rm g}$-$M_\star$ relation is required for the star formation efficiency to increase with stellar mass.

mation. This closely resembles so-called "cold-mode" accretion scenario in which gas falling into lower mass halos along filaments do not experience significant shock-heating, thereby easily accreting onto the central galaxy (Dekel & Birnboim 2006; Kereš et al. 2005, 2009; Dutton et al. 2010b). At higher masses, on the other hand, accreting gas may be shock-heated and subsequently unable to cool and contribute to star formation. Despite this neat picture, however, we find it intriguing that $f_{\rm cold}(M_\star)$ is so close to unity at low masses. Figure 2 clearly shows that $M_\star + M_{\rm g}$ in these same galaxies falls short of accounting for all of the baryons in the halo by at least a factor of two. Thus, a large part of the accreted baryons must be removed from the halo via strong winds, even if the star formation is reasonably inefficient in these galaxies, possibly induced by a particularly strong supernova feedback efficiency.

Finally, Figure B3 builds on this analysis to show the star formation efficiency, traditionally-defined as $\dot{M}_{\rm SFR}/M_{\rm g}$, as a function of stellar mass for the total cold gas fractions and the three choices of SSFR. In all cases, star formation is more efficient in more massive galaxies: they are forming more stars per unit gas (though see Schiminovich et al. 2010). Several previous analyses of the mass-metallicity relation have suggested that a varying star formation efficiency with galaxy mass is required in order to reproduce the mass-metallicity relation (e.g., Brooks et al. 2007; Calura et al. 2009). Figure B3 shows that this condition is implicitly passed as long as gas fractions are decreasing with galaxy mass and star formation rates vary reasonably with stellar mass, as is observed for $z = 0$ galaxies. We note, however, that with proper choices of $\zeta_{\rm w}$, the mass-metallicity relation is *theoretically* able to be reproduced with a constant $F_{\rm g}$ and therefore constant star formation efficiency.